Research Square

Preprints are preliminary reports that have not undergone peer review.
They should not be considered conclusive, used to inform clinical practice,
or referenced by the media as validated information.

Spatial characteristic of temperature distribution and material flow behaviors during bobbin tool friction stir welding: a computational fluid dynamics study

Honghua Han
Tsinghua University
Xu Yan
Capital Aerospace Machinery Company
Yanhua Zhao
Capital Aerospace Machinery Company
Suhong Zhang
Capital Aerospace Machinery Company
Qingyu Shi
Tsinghua University
Chengle Yang
Tsinghua University
Yunfei Hao
Capital Aerospace Machinery Company
Gaoqiang Chen
cheng1@tsinghua.edu.cn

Tsinghua University

Research Article

Keywords: Bobbin tool friction stir welding, Contact model, Temperature field, Material flow, Numerical simulation

Posted Date: September 8th, 2026

DOI: https://doi.org/10.21203/rs.3.rs-10650061/v1

License: This work is licensed under a Creative Commons Attribution 4.0 International License.
Read Full License

Additional Declarations: No competing interests reported.

Spatial characteristic of temperature distribution and material flow behaviors during bobbin tool friction stir welding: a computational fluid dynamics study

Honghua Han[1,2], Xu Yan[3], Yanhua Zhao[3], Suhong Zhang[3], Qingyu Shi[1], Chengle Yang[1], Yunfei Hao [3,*], Gaoqiang Chen[1,*]

1. State Key Laboratory of Clean and Efficient Turbomachinery Power Equipment, Department of Mechanical Engineering, Tsinghua University, Beijing 100084, China

2. Beijing Vocational College of Labour and Social Security, Beijing 100029, China

3.Capital Aerospace Machinery Company，Beijing 100076，China

*Corresponding authors: Yunfei Hao,email: haoyunfei1234@163.com

Gaoqiang Chen, email: cheng1@tsinghua.edu.cn

Abstract

The incorporation of dual shoulders endows bobbin tool friction stir welding (BT-FSW) with spatially distinct heat transfer and material flow characteristics relative to conventional FSW. The vague understanding of these processes hinders efficient optimization of BT-FSW. To address this gap, a computational fluid dynamics (CFD) model, which considered the fully coupling of thermo-mechanical-fluid, was established. Three contact pressure models, namely the Front-Peaked Contact Pressure Model (FP-CPM), Uniform Contact Pressure Model (U-CPM), and Rear-Peaked Contact Pressure Model (RP-CPM), were proposed to model the pressure distribution at the tool-workpiece (T/W) interface. The results show that the distribution of contact pressure at the T/W interface constitutes a critical factor governing the temperature field and flow behavior during welding stage. The FP-CPM provided superior predictive accuracy for the welding temperature, the shape of plastic deformation zone, and material flow trajectories, compared to U-CPM and RP-CPM. Agreed by both experiment and prediction, the temperature on the retreating side (RS) exceeded that on the advancing side (AS). Revealed by FP-CPM model, this phenomenon is attributable to the deflection of high-temperature material from the AS toward the RS, driven by the intense material flow ahead of the tool

induced by the high-pressure zone. At the T/W interface, the material exhibited asymmetric horizontal flow with a thin layer ahead of the tool and a broader low-speed region behind the tool. Concurrently, vertical migration featured circumferential flow around the tool converging toward the plate mid-thickness.

Keywords: Bobbin tool friction stir welding; Contact model; Temperature field; Material flow; Numerical simulation

1. Introduction

Bobbin tool friction stir welding (BT-FSW) represents an advanced variant of conventional friction stir welding (FSW), a solid-state joining technology [1]. The BT-FSW tool features dual shoulders, with the lower shoulder serving as a substitute for the rigid backing anvil required in conventional FSW, thereby enabling welding operations without back-side support [2]. Through the simultaneous rotation and traverse motion of the shoulders and pin, BT-FSW achieves coupled thermo-mechanical loading, which plasticizes the material and induces flow. This process effectively mitigates root defects such as weak root bonding, facilitates the formation of sound welds, and extends the applicability of welding to large-scale hollow structures and complex curvilinear geometries[3-5]. However, the increased thermal input renders the weld susceptible to defect formation.[6]. Consequently, heat input and the involved material flow during BT-FSW constitute decisive factors governing weld formation quality [2,7,8].

Numerical simulation has been proven to be an effective approach to reveal the underlying mechanism during FSW and its variant[9-11]. Early research efforts have established various computational models, encompassing fundamental heat transfer models [12,13], flow models [11,14,15], and fully coupled thermo-mechanical-fluid models [16-18]. The prevailing consensus holds that interaction at the tool-workpiece (T/W) interface serves as the dominant heat source, while elevated temperatures reduce the material flow stress, thereby generating intense plastic deformation heat[10,19-21]. Therefore, the contact pressure distribution and interfacial interaction at the T/W interface govern heat generation and transfer, and subsequently influence material flow behavior. Extensive theoretical and experimental investigations have addressed the temperature field in

conventional FSW [22,23]. In conventional FSW process, the thermal asymmetry is typically manifested as higher temperatures on the advancing side (AS) compared with the retreating side (RS) [20,24-29]. For instance, Yin et al. [30] elucidated through numerical modeling that the elevated AS temperature arises from the maximum shear rate occurring on the AS and the minimum on the RS. Consequently, material on the AS undergoes more severe deformation under the rotational and extrusive action of the pin, resulting in greater viscous dissipation heating. Some researchers have further attributed this thermal asymmetry to the tool tilt angle in conventional FSW. Zhang et al. [24] demonstrated that variations in tool tilt angle induce differential friction force distributions, which exert a pronounced influence on the temperature field and material flow. Both their experimental measurements and predictive models confirmed that a 2.5° tilt angle yields higher temperatures on the AS than on the RS. Wu et al. [31] observed similar asymmetric temperature distributions under identical tilt angle conditions. In summary, the contact pressure distribution and interfacial interaction at the T/W interface govern heat generation and transfer, whereas thermal asymmetry characterizes the FSW process.

However, the physical mechanisms responsible for thermal asymmetry in BT-FSW remain controversial [2,32-35]. Specifically, the dominant factors determining whether the AS or the RS exhibits higher temperatures remain unclear, and a unified explanation for the origin of this asymmetry is still lacking, thereby constraining a thorough understanding of material flow behavior. One view holds that during tool rotation and forward translation, material on the AS is subjected to shear stresses that drive material transfer from the AS toward the RS, thereby resulting in higher temperatures on the RS than on the AS. Feng et al. [36] observed in BT-FSW experiments that the peak temperature on the RS exceeded that on the AS by approximately 20 °C. The authors attributed this phenomenon to the rotation-induced transfer of plasticized metal and partial thermal energy from the AS toward the RS, which led to lower temperatures on the AS. However, they did not elucidate the underlying cause of the elevated RS temperature through numerical simulation. Li et al. [33] reported similar experimental findings. Conversely, an opposing view argues that the AS experiences greater shear stresses, thereby facilitating the generation of higher temperatures on the AS. Sun et al. [34] conducted BT-FSW experiments on T2 pure copper and found that the peak temperature on the AS (422 °C) exceeded that

on the RS (352 °C) at a position 2 mm from the weld center. The authors attributed this observation to the greater stresses sustained by plasticized material on the AS, which generated more friction-induced heat and consequently produced a higher peak temperature. These results confirm the asymmetric temperature distribution in BT-FSW, though the governing physical mechanisms have yet to be fully clarified.

It should be noted that some researchers have merely presented experimental or numerical results without conducting a more in-depth analysis of the observed temperature discrepancies. Li et al. [35] performed BT-FSW experiments on ZK60 magnesium alloy and conducted numerical simulations based on the Eulerian-Lagrangian method. At a location 7 mm from the weld center, the RS temperature exceeded the AS temperature by 70 °C. However, the authors did not provide an explanation for the origin of this temperature difference. Feng et al. [2] investigated the influence of BT-FSW on joint temperature in 6061-T6 aluminum alloy plates. Experimental results indicated that the peak temperature on the RS was higher than that on the AS. The authors also employed COMSOL multiphysics simulation software, which yielded peak temperatures approximately 10 °C higher than the measured values. Nevertheless, they did not clarify whether the simulation results exhibited the same phenomenon of higher RS temperatures. Zhao et al. [37] proposed a pressure-dependent velocity boundary condition based on wear theory [38]. This novel model effectively captured the influence of welding speed on weld cross-sectional geometry and predicted higher temperatures on the RS than on the AS. However, the predicted temperature difference reached 70 °C. The authors explained that the low-pressure zone restricted material flow on the AS, whereas flow on the RS was more pronounced, resulting in a distorted velocity field morphology that elevated the RS temperature. In contrast, their comparative simulation employing a velocity model produced the opposite result, namely higher temperatures on the AS than on the RS. Singh et al. [32] developed a sliding-sticking contact mechanism for the T/W interface in BT-FSW using a CFD-based approach with a variable friction coefficient. Their results indicated higher temperatures on the AS than on the RS, and the velocity field exhibited axisymmetric characteristics. The above studies indicate that precise matching of temperature measurement data with numerical simulation results, and the subsequent accurate prediction of asymmetric temperature field distributions in BT-FSW, currently remain challenging.

Recent studies have demonstrated that the coupled frictional shear-stress boundary model developed by Chen et al. [39] accurately captures the interfacial interaction at the T/W interface. In some previous investigations, the contact pressure at the T/W interface was assumed constant [20,28,40]. However, existing experimental and numerical studies have revealed that the contact pressure at the T/W interface is non-uniformly distributed [19,41-45], which induces variations in the temperature and velocity fields. Zhang et al. [41] found that the forward-directed force acting on the tool arises primarily from non-uniform contact pressure. The contact pressure at the tool front significantly exceeds that at the rear and correlates with both rotational speed and welding speed: higher rotational speeds reduce the front-rear pressure differential, whereas higher welding speeds amplify it. Zhang et al. [42] further developed a CFD model to obtain the pressure distribution pattern and elucidated the influence of tool rotational speed and welding speed on peak temperature. Pei et al. [45] incorporated contact behavior between the pin and the material, and accounted for heating effects at the shoulder-workpiece interface and contact interactions between the pin and the workpiece. Shi et al. [19] proposed a contact pressure distribution model correlated with the angle between the radius vector and the welding direction. This model successfully captures the variation in contact pressure differential around the tool. Dialami et al. [43] modified Norton's friction law by introducing a consistency parameter a(x,T). Their results demonstrated that the material velocity field exhibited a non-uniform distribution. At the front of the shoulder, high contact pressure maintained the material in a sticking state, whereas sliding occurred at the rear. This stick-slip transition altered the heat generation distribution, and the predicted temperatures on the AS and RS agreed closely with experimental measurements. Some researchers have also identified tool tilt angle as a factor inducing non-uniform contact pressure in conventional FSW. The tilt angle exerts a significant influence on stress, temperature, plastic deformation, and material flow velocity during the process [24,46-48]. The above studies demonstrate that the contact pressure at the T/W interface exhibits a pronounced non-uniform distribution, with the pressure at the tool front significantly exceeding that at the rear, and this distribution correlates with both rotational speed and welding speed, thereby inducing variations in the temperature and velocity fields.

In summary, the complex interaction mechanisms at the T/W interface in BT-FSW have resulted

in incompletely elucidated spatial characteristics of the temperature field and material flow; therefore, numerical simulation is necessary to further reveal the underlying mechanisms of heat generation, heat transfer, and material flow. Accordingly, this study proposed two non-uniform contact pressure model incorporating T/W interfacial interaction, and compares them to a conventional model with uniformly distributed pressure. The models were separately integrated into a fully coupled thermo-mechanical-fluid numerical method based on CFD to quantitatively analyze the influence of welding parameters on the thermo-mechanical coupling process. The simulation results were thoroughly validated by comparing to experimental measurement of welding temperature, morphology of stir zone, and the distribution of marker material in the joint.

2. Welding experiment

The workpiece material employed in the BT-FSW experiments was 2219-T8 aluminum alloy. Two plates of identical dimensions were joined in a butt configuration. Each plate measured 300 mm in length, 100 mm in width, and 6 mm in thickness. The experiments were conducted on an FSW-5M friction stir welding apparatus manufactured by Shanghai Top Numerical Control Technology Co., Ltd. The welding experimental procedure is illustrated in Fig. 1.The tool featured upper and lower shoulders each 20 mm in diameter. Both shoulders were designed with a convex arc-shaped profile. Compared with the conventional planar shoulder configuration, this convex geometry offered superior upsetting force and better accommodated shoulder penetration. The pin diameter was 10 mm. The upper section of the pin carried a left-hand thread, whereas the lower section carried a right-hand thread. The tool rotational speed was 300 rpm, and the welding speed was 250 mm/min. The coordinate system was defined with the origin O located at the intersection of the tool central axis and the bottom surface of the workpiece. The welding direction corresponded to the negative X-direction. The Y-axis was oriented perpendicular to the weld seam, and the Z-axis pointed toward the upper surface of the workpiece. To visualize material flow behavior, a copper foil 0.1 mm in thickness was inserted at the butt interface between the two plates. After welding, the copper tracer distribution was examined using a ZXFlasee S-type X-ray digital imaging system. Four temperature measurement points, designated P1, P2, P3, and P4, were symmetrically positioned on both sides of the weld centerline on the top

surface. The spacing between P1 and P4 was 28 mm, and that between P2 and P3 was 24 mm. The measurement points comprised blind holes 1 mm in diameter and 2 mm in depth for the installation of K-type thermocouples. Temperature data were recorded during the experiments using an LR8450-01 data logger manufactured by HIOKI Corporation at a sampling frequency of 50 Hz. After welding, specimens were extracted from the transverse cross-section of the welded joint. The samples were ground and polished, and subsequently etched in Keller's reagent by immersion for 15 s. The macrostructural morphology of the welded joint was then examined.

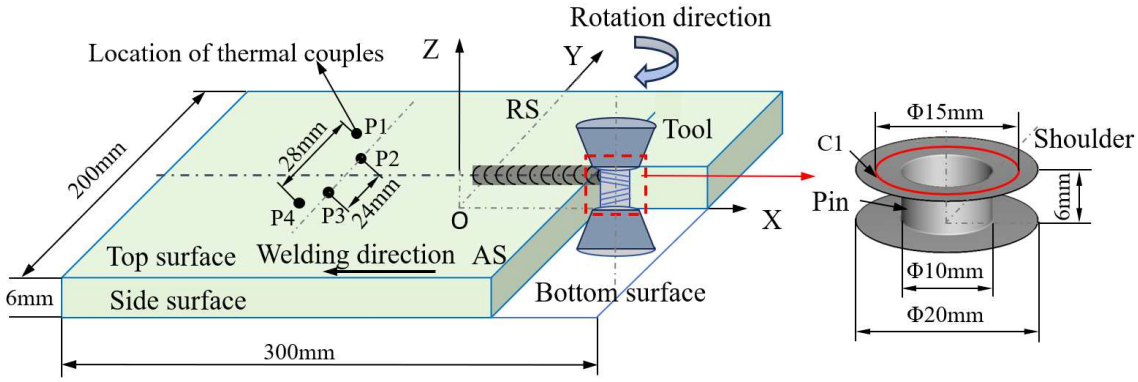


Fig.1 Illustration of the BT-FSW process

3. The Fully coupled thermo-mechanical-fluid model

3.1. Geometric model and mesh generation

Fig 2 presents the geometric model and mesh generation employed in the BT-FSW numerical simulation. The geometric model dimensions were identical to those of the experimental workpiece. A hexahedral structured mesh was employed. To ensure consistency in the computational results, the mesh comprised 360,240 elements. Extremely high temperature and velocity gradients exist at the T/W interface and in its vicinity, so the mesh in this region was refined. The minimum mesh size was 0.2 mm. The shoulder penetration depth was set to 0.2 mm for both the upper and lower shoulders. When the tool advances along the welding direction and rotates, tangential friction forces and pressures normal to the thread surface are generated at the interface between the threaded pin and the material. These pressures are directed toward the plate mid-thickness [49,50]. To simulate the influence of the threaded pin on material flow, the method proposed by the present authors for superimposing thread-interface velocities on a cylindrical pin was adopted [51]. The welding speed and rotational speed specified in the geometric model were identical to those used in the experiments. Mesh generation was

performed using ANSYS Workbench Meshing. The simulations were conducted using the FLUENT solver. Boundary conditions were defined through user-defined functions (UDFs) compiled in the C programming language.

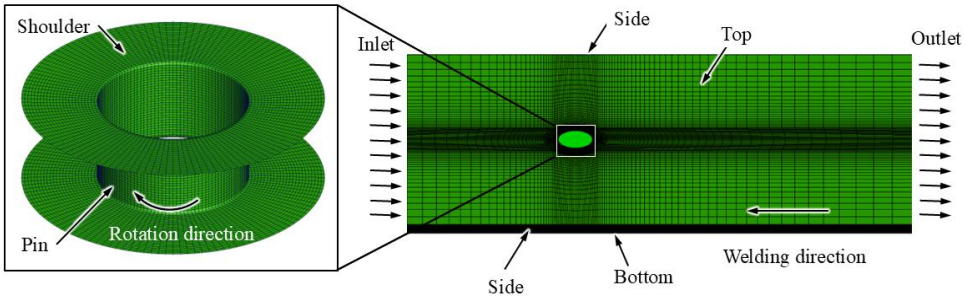


Fig. 2 Geometric modeling and meshing

3.2 Governing equations

In the CFD model, the workpiece material was treated as an incompressible single-phase non-Newtonian viscous fluid. The coupled multi-physics governing equations consist of the continuity equation, the momentum conservation equation, and the energy conservation equation.

The continuity equation:

$$\frac{\partial \rho}{\partial t} + \nabla \cdot \left(\rho \vec{\boldsymbol{v}} \right) = 0 \tag{1}$$

The momentum conservation equation:

$$\frac{\partial \rho \vec{\boldsymbol{v}}}{\partial t} + \nabla \cdot \left(\rho \vec{\boldsymbol{v}} \vec{\boldsymbol{v}} \right) = -p + \nabla \cdot \left(\mu \left(\nabla \vec{\boldsymbol{v}} + \nabla \vec{\boldsymbol{v}}^{T} \right) \right) \tag{2}$$

The energy conservation equation:

$$\frac{\partial \rho H}{\partial t} + \nabla \cdot \left(\rho \vec{\boldsymbol{v}} H \right) = \nabla \cdot \left(\lambda \nabla T \right) + S_v \tag{3}$$

where ρ is the density of the workpiece material, assigned a value of 2840 kg/m³ [52]. The flow field is described by the velocity vector $\vec{\boldsymbol{v}}$, flow time t and pressure p. The material's thermal and mechanical properties include the non-Newtonian viscosity μ (a function of temperature T) and the thermal conductivity λ. Finally, S_v represents the heat source due to plastic deformation, and H is the enthalpy, defined as:

$$H = \int_{T_{ref}}^{T} C_p \mathrm{d}T \tag{4}$$

where C_p is the specific heat capacity, and T_{ref} is the ambient temperature, set to 27 °C in the

present model.

3.3. Frictional Boundary Conditions

In the fully coupled BT-FSW model, interfacial interaction at the T/W interface constitutes a critical component of the mathematical formulation [19]. The present study adopted the shear stress boundary model proposed by Chen et al. [39], which accounted for the transition between sliding and sticking states of the material at the T/W interface. The frictional shear stress exerted by the tool on the workpiece was expressed as [28]:

$$\vec{\tau}_f = \mu_f P(\theta, R) \frac{\vec{\boldsymbol{v}}_{rel}}{\left\| \vec{\boldsymbol{v}}_{rel} \right\|} \tanh\left(\alpha \vec{\boldsymbol{v}}_{rel} \right) \tag{5}$$

where μ_f denotes the friction coefficient, assigned a value of 0.5 [39], $P(\theta, R)$ is the contact pressure at the T/W interface, as illustrated in Fig. 3; θ is the angle between the X-axis and the contact pressure $P(\theta, R)$, as shown in Fig. 4; R is the radial distance from the tool center to a point on the shoulder surface, expressed in the Cartesian coordinate system as $R = \sqrt{x^2 + y^2}$. Following Ref. [46], the present study defined the contact area as S, assuming full contact between the shoulder surface and the material with no non-contact regions. $\vec{\boldsymbol{v}}_{rel}$ denotes the relative velocity of the material at the T/W interface, defined as $\vec{\boldsymbol{v}}_{rel} = \vec{\boldsymbol{v}}_{tool} - \vec{\boldsymbol{v}}_{mat}$, $\vec{\boldsymbol{v}}_{tool}$ is the tool motion velocity, $\vec{\boldsymbol{v}}_{mat}$ is the material velocity at the T/W interface; and α is the control factor, assigned a value of 50 s/m [39]. Previous studies have demonstrated that various assumed distributions of contact pressure at the T/W interface exist. The first view holds that during tool rotation and continuous traverse, the material ahead of the tool sustains greater compressive pressure, whereas the material behind the tool experiences reduced pressure [53]. The material in front of the tool is subjected to more pronounced shear action, indicating the existence of non-uniform contact pressure at the T/W interface, with the front-end contact pressure exceeding that at the rear [41,42,45,54]. The second pressure distribution form assumes a constant contact pressure (Fig. 3b). The third view argues that in conventional FSW, the introduction of a tilted tool produces higher axial force behind the tool than ahead of it [24], thereby altering the temperature field distribution and material flow. To facilitate a comparative investigation of the influence of tool contact pressure distribution on the spatial characteristics of the temperature field and material flow

behavior, and to provide a corroborative rationale for the present approach, the present study referenced the effect of tool tilt angle on shoulder pressure in FSW [24,46,48], the generation of additional upsetting force at the rear of the tool [46,47], and the influence of welding speed and rotational speed on contact pressure [19,41]. Accordingly, the present study adopted three distinct interfacial contact pressure models. The first model featured a non-uniform contact pressure distribution characterized by higher pressure ahead of the tool than behind it, designated as the Front-Peaked Contact Pressure Model (FP-CPM) (Fig. 3a). The second model assumed a uniform contact pressure distribution, designated as the Uniform Contact Pressure Model (U-CPM) (Fig. 3b), in which the contact pressure was set to 46.7 MPa [20,55]. The third model also featured a non-uniform contact pressure distribution, but with higher pressure behind the tool than ahead of it, designated as the Rear-Peaked Contact Pressure Model (RP-CPM) (Fig. 3c).

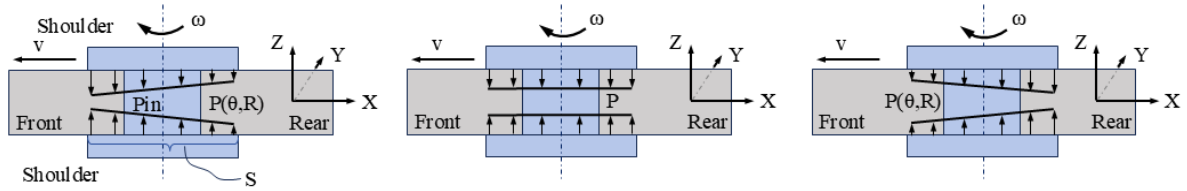


Fig. 3 Schematic of pressure distributions for the three CPMs

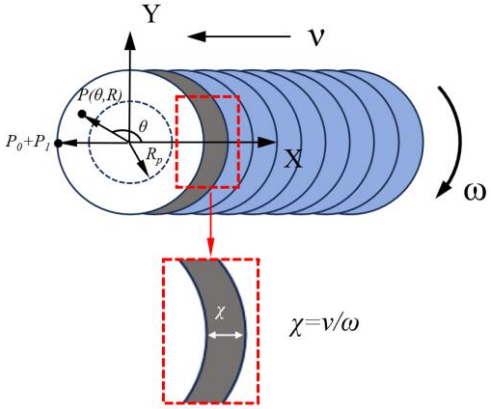


Fig. 4 Schematic of the non-uniform contact pressure ahead of the tool in the FP-CPM

As shown in Fig. 4, $\chi = v/w$ denotes the advance distance of the tool per revolution [19,54]. A general expression for the contact pressure factor correlated with χ and θ was defined as:

$$y(\chi,\theta) = \frac{1}{\sqrt{\chi \cdot (1 \pm \cos\theta)^2 + 1}} \tag{6}$$

The positive sign indicates that the contact pressure factor reaches its maximum at $\theta = \pi$, simulating the contact pressure of the FP-CPM. The negative sign indicates that the contact pressure factor reaches its maximum at $\theta = 0$, simulating the contact pressure of the RP-CPM. Equation (6) was normalized as:

$$y^*(\chi,\theta) = \frac{y(\chi,\theta) - y_{\min}(\chi,\theta)}{y_{\max}(\chi,\theta) - y_{\min}(\chi,\theta)} \tag{7}$$

Therefore, a non-uniform contact pressure distribution model correlated with welding speed, rotational speed, angle, and radius was adopted to reflect the contact pressure at the T/W interface. The expression is given as:

$$P(\theta,R) = P_0 \cdot y^*(\chi,\theta) + P_1 \cdot \left(\frac{R - R_p}{R_s - R_p}\right)^a \tag{8}$$

where P_0 is the maximum contact pressure correlated with welding speed, tool rotational speed, and angle. R_s is the maximum shoulder radius, and R_p is the pin radius. P_1 is the maximum contact pressure correlated with *R*, and a is the radius correlation coefficient, assigned a value of 1.0. To ensure consistency of the upsetting force acting on the three CPMs, Equations (6) through (8) were combined, and the upsetting force was expressed as:

$$F = \int_0^{2\pi} \int_{R_p}^{R_s} P(\theta,R) d\theta dR \tag{9}$$

The frictional shear stress formulation was established through Equations (5) to (8). Fig. 5 presents the frictional shear stress distributions in the FP-CPM and RP-CPM. The distributions demonstrate that the frictional shear stress varies with angle θ and radius R. In the FP-CPM (Fig. 5a), the combined contact pressure at the front of the tool produces a maximum peak frictional shear stress (i.e., $P_0 + P_1$), while the frictional shear stress at the rear of the tool decreases to its minimum value. Fig. 5b presents the RP-CPM contact pressure distribution, which is opposite to that in Fig. 5a. The frictional shear stress is low ahead of the tool and high behind it. Under the uniform contact pressure of the U-CPM, the frictional shear stress remains constant; therefore, its contour plot is omitted. Fig. 6 presents the variations of pressure and frictional shear stress with θ for the three CPMs at the position of Curve C1 shown in Fig. 1. The results indicate that the FP-CPM and RP-CPM successfully capture the variation trends of contact pressure and frictional shear stress at the T/W interface with θ and *R*. The

U-CPM exhibits uniform distributions of pressure and frictional shear stress.

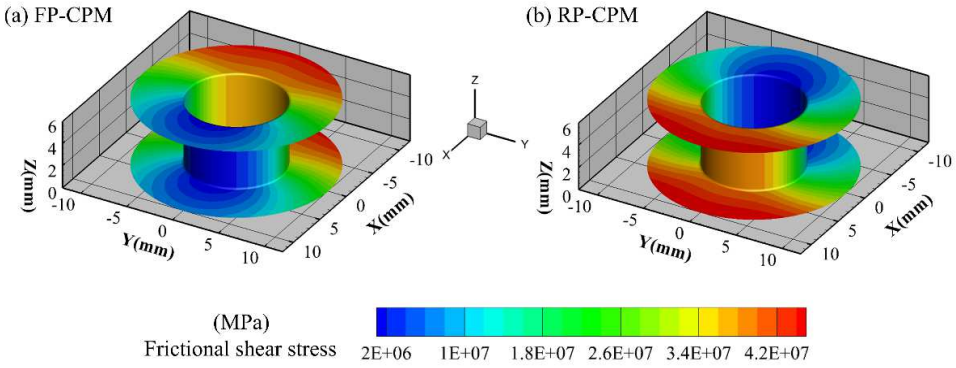


Fig. 5 Frictional shear stress distributions in the FP-CPM and RP-CPM

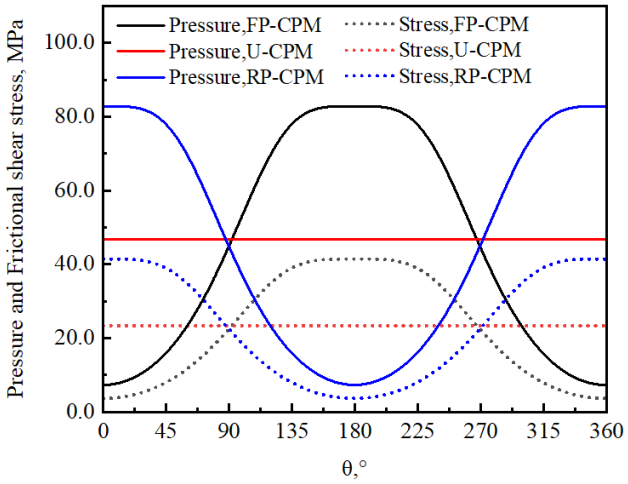


Fig. 6 Contact pressure and frictional stress distributions for the three CPMs

3.4. Contact Condition at the T/W Interface

During the welding process, three distinct contact conditions exist at the tool-workpiece (T/W) interface: full sliding, partial sliding-sticking, and full sticking [12]. Consequently, these different contact conditions lead to pronounced variations in the physical fields at the interface, particularly the velocity field and the temperature field. To characterize the contact condition of the material at the T/W interface, a slip rate δ is introduced to describe the material flow behavior (Eq. (10)). It is defined such that the material at the T/W interface exhibits full sliding when δ = 1, full sticking when δ = 0, and partial sliding-sticking when 0 < δ < 1 [21].

$$\delta = \frac{\left\| \vec{v}_{ref} \right\|}{\left\| \vec{v}_{tool} \right\|} \tag{10}$$

3.5. Heat Generation Model

During the BT-FSW process, welding heat input is generally considered to originate from two sources: frictional heat generation at the T/W interface and heat produced by plastic deformation through the conversion of plastic work[2]. Frictional heat generation constitutes a surface heat source. The expression for the heat flux density is given as [28,52]:

$$q_f = \eta \left\| \vec{\boldsymbol{\tau}}_f \right\| \left\| \vec{\boldsymbol{v}}_{ref} \right\| \tag{11}$$

$$\eta = \frac{\sqrt{(\lambda \rho C_p)}_w}{\sqrt{(\lambda \rho C_p)_w} + \sqrt{+(\lambda \rho C_p)_T}} \tag{12}$$

where η is the frictional heat partition coefficient, representing the proportion of heat generated by the tool that flows into the workpiece material. A value of 0.7 was adopted in the present study [20,56]. The subscripts T and W denote the tool and the workpiece, respectively.

The heat generation expression for plastic deformation is given as [57]:

$$q = \beta \cdot \bar{\sigma} \cdot \dot{\varepsilon} \tag{13}$$

where β is the thermal dissipation coefficient of plastic work. A value of 0.76 was adopted in the present study following Ref. [58]. $\bar{\sigma}$ is the material flow stress, and $\dot{\varepsilon}$ is the equivalent strain rate.

3.6. Thermal Boundary Conditions

Heat dissipation at the top and bottom surfaces and the side walls of the workpiece was described by a unified heat transfer equation expressed in the general form [51]:

$$\lambda \frac{\partial T}{\partial \vec{n}_b} = h\left(T - T_0\right) \tag{14}$$

where $\vec{n}_b$ is the unit normal vector perpendicular to the boundary surface, $\frac{\partial T}{\partial \vec{n}_b}$ is the temperature gradient in the normal direction near the boundary, h is the heat transfer coefficient, and T_0 is the initial temperature, set to 27 °C. No backing plate was employed beneath the workpiece; accordingly, the convective heat transfer coefficients at the top and bottom surfaces exposed to ambient air were specified as 20 W/(m²·K) [6,59]. The side walls were in contact with the fixture, and the contact heat transfer coefficient was assigned a value of 200 W/(m²·K) [6,35].

3.7 Material Constitutive Model

C_p and λ were defined as temperature-dependent functions, with values adopted from Ref.

[60], as shown in Fig. 7. The Sellars-Tegart constitutive model was employed to describe the high-temperature flow behavior of the aluminum alloy during the welding process, as this model is widely adopted for characterizing flow stress under elevated temperature conditions. The mathematical expression for the flow stress is given as:

$$\overline{\sigma} = \sigma_p \cdot \sinh^{-1}\left[\left(\frac{Z(T,\dot{\varepsilon})}{A}\right)^{\frac{1}{n}}\right] \tag{15}$$

where the Zener-Hollomon parameter Z is defined as:

$$Z\left(T,\dot{\varepsilon}\right) = \dot{\varepsilon} \cdot \exp\left(\frac{Q}{RT}\right) \tag{16}$$

$$\dot{\varepsilon} = \left(\frac{2}{3}\varepsilon_{ij} \cdot \varepsilon_{ij}\right)^{\frac{1}{2}} \tag{17}$$

$$\varepsilon_{ij} = \frac{1}{2}\left(\frac{\partial u_i}{\partial x_j} + \frac{\partial u_j}{\partial x_i}\right) \tag{18}$$

In Equations (15) through (18), ε_{ij} denotes the strain rate tensor. u_i and u_j are the velocity vector components; x_i and x_j are the three-dimensional spatial coordinates. R is the ideal gas constant, with a value of 8.314 J/(mol·K), and Q is the activation energy for deformation, assigned a value of 123320 J·mol^{-1}. Material constants A, n, and σ_p were determined by fitting to high-temperature compression experimental data, with values adopted from Ref. [61]: A = 1.36 × 10^9 s^{-1}, n = 5.65, H = 76.92 MPa, and σ_h = 110 MPa. A softening correction was applied to the flow stress in the high-temperature region [52,57]. Based on this model, a quantitative correlation was established between the high-temperature flow behavior of the material and the process parameters (rotational speed, welding speed, etc.). The material viscosity was expressed as [59,62]:

$$\mu = \frac{\overline{\sigma}}{3\dot{\varepsilon}} \tag{19}$$

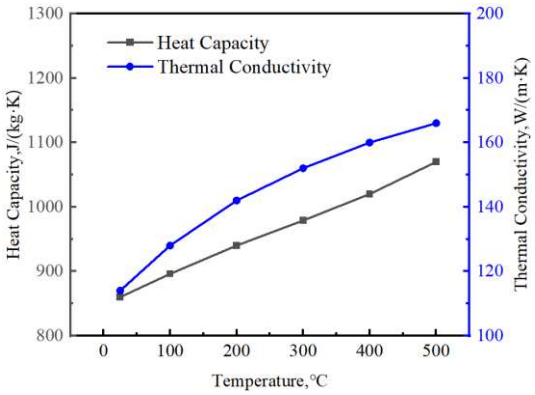


Fig. 7 heat capacity and thermal conductivity

4. Results and Discussion

4.1. Temperature field during the welding process

Fig. 8 presents the simulation results of the temperature distribution on the top surface of the workpiece. During the welding process, all three models exhibited a markedly higher temperature gradient ahead of the tool than behind it, which is consistent with the typical characteristics of welding temperature fields. The peak temperature for the FP-CPM was 485.9 °C, located on the RS of the tool; that for the U-CPM was 500.6 °C, located on the AS; and that for the RP-CPM was 495.5 °C, located behind the tool. The peak temperatures under all three CPMs were below the solidus temperature of 2219 aluminum alloy (543 °C), indicating that the material remained in the solid state throughout the welding process. This is consistent with the fundamental nature of FSW as a solid-state joining technology.

Fig. 9 presents the temperature contour maps on the X = 0 cross-section for the three CPMs. The temperature contours near the T/W interface assumed a dumbbell-shaped distribution for all three CPMs. The temperatures near the upper and lower shoulders were higher than those near the pin. The thermal symmetry between the upper and lower shoulders contributes to a more balanced heat input into the weld and is conducive to improved mechanical performance of the joint. In the FP-CPM, the RS temperature was higher than that on the AS, whereas in the U-CPM and RP-CPM, the AS temperature exceeded that on the RS. To evaluate the accuracy of the temperature field simulation, the simulation data were compared with the experimental temperature measurements.

Fig. 10 presents the comparison between the simulated and measured temperatures at the four points P1 through P4 for the three CPMs, as illustrated in Fig. 1. All monitoring points exhibited rapid

temperature rise as the tool passed and subsequent gradual cooling. The temperature variation trends were consistent with the observed experimental temperature histories. Figs. 10a and 10b reveal that the predicted temperatures at points P1 through P4 in the FP-CPM exhibited a pattern of higher temperatures on the RS than on the AS. Specifically, the predicted peak temperatures at P1 and P2 exceeded those at P4 and P3, respectively. This predicted phenomenon of higher RS temperatures than AS temperatures is in excellent agreement with the experimental measurements. Figs. 10c through 10f reveal that the predicted temperatures at points P1 through P4 in the U-CPM and RP-CPM exhibited a pattern of higher temperatures on the AS than on the RS. Specifically, the predicted peak temperatures at P1 and P2 were lower than those at P4 and P3, respectively, indicating substantial deviation from the experimental temperatures. This indicates that the FP-CPM, constructed on the basis of a non-uniform contact pressure distribution, accurately captures the temperature field distribution during the BT-FSW process and achieves high predictive accuracy for the temperature field.

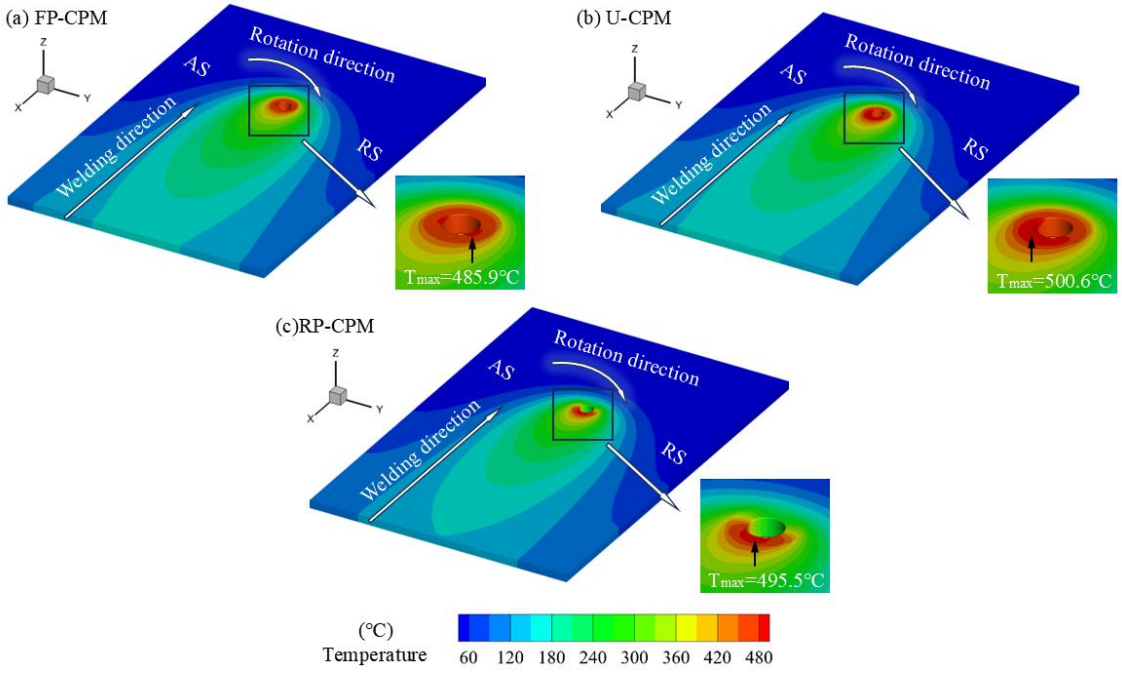


Fig. 8 Temperature distribution contours

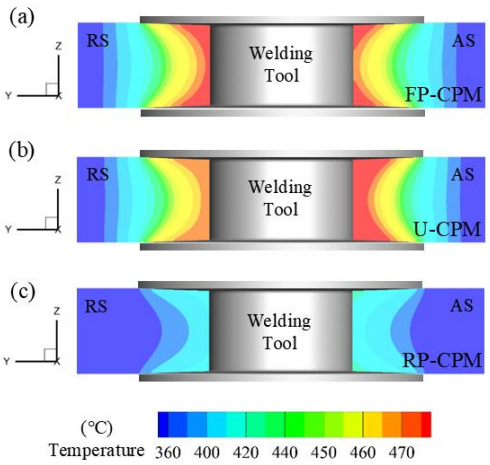


Fig. 9 Temperature contours at X = 0 mm cross-section

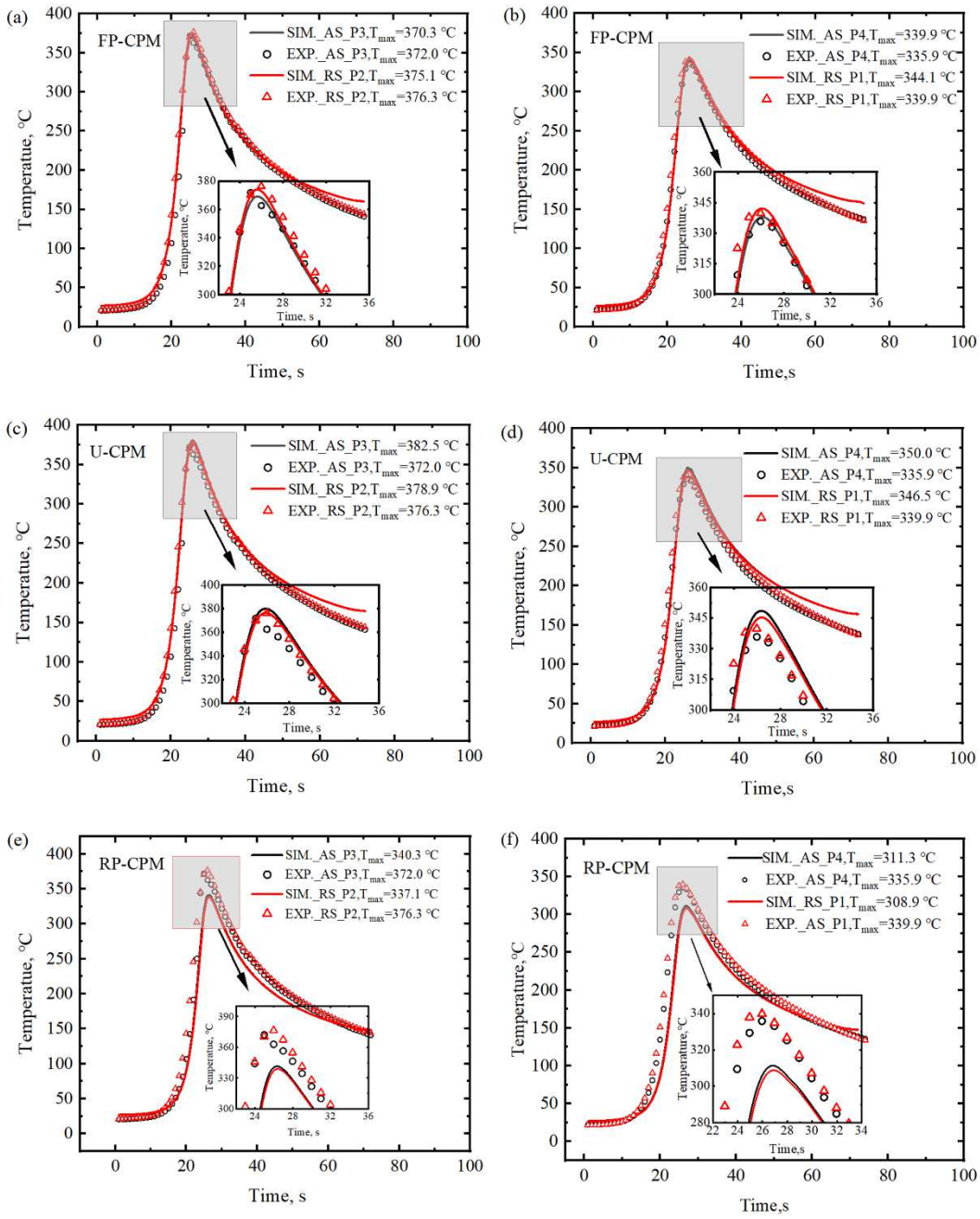


Fig. 10 Comparison of simulated and measured temperatures

(a) P2 and P3 in FP-CPM. (b) P1 and P4 in FP-CPM. (c) P2 and P3 in U-CPM. (d) P1 and P4 in U-CPM. (e) P2 and P3 in RP-CPM. (f) P1 and P4 in RP-CPM.

To further analyze the spatial distribution characteristics of the temperature field around the tool, Fig. 11 presents the positions of Curves C2 through C5 around the plate mid-thickness plane (Z = 3 mm), indicated by red dashed lines. The specific coordinates of the starting and ending points for the four curves are provided in Table 1. Fig. 12 presents the comparison of temperature distributions along

Curves C2 through C5 under the three models. The FP-CPM and U-CPM exhibited temperatures of 364.4 °C and 349.2 °C, respectively, at the coordinate (−10, 0, 3), which corresponds to the starting point of Curve C2. At the coordinate (−5, 0, 3), which corresponds to the ending point of Curve C2, the temperatures were 464.4 °C and 461.2 °C, respectively. Under both models, the temperature gradients at the front position were relatively large. A horizontal line is drawn through the maximum temperature point on Curve C4 in the figure, indicated by the black dashed line. In the FP-CPM, the peak temperature on Curve C5 exceeded that on Curve C4, whereas in the U-CPM and RP-CPM, the peak temperature on Curve C5 was lower than that on Curve C4. This indicates that the FP-CPM consistently exhibits a spatial distribution of higher temperatures on the RS than on the AS around the tool. The temperature of Curve C3 in the U-CPM and RP-CPM was significantly higher than that in the FP-CPM, indicating that the temperature behind the tool exceeds that ahead of the tool in these two models. This is markedly distinct from the FP-CPM.

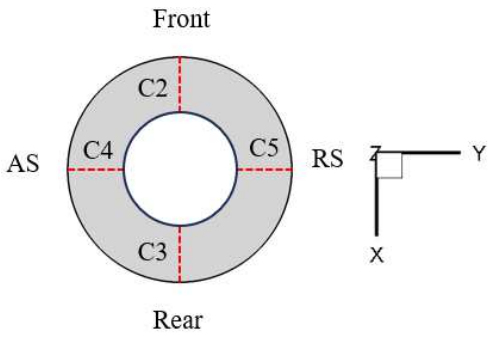


Fig. 11 Schematic of curves C2 – C4 on the tool mid-plane (Z = 3 mm)

Table1 Positions of Start and End Points for Curves C2 – C5 (mm)

No.	Start Coordinates	End Coordinates
C2	(-10,0,3)	(-5,0,3)
C3	(5,0,3)	(10,0,3)
C4	(0,-10,3)	(0,-5,3)
C5	(0,5,3)	(0,10,3)

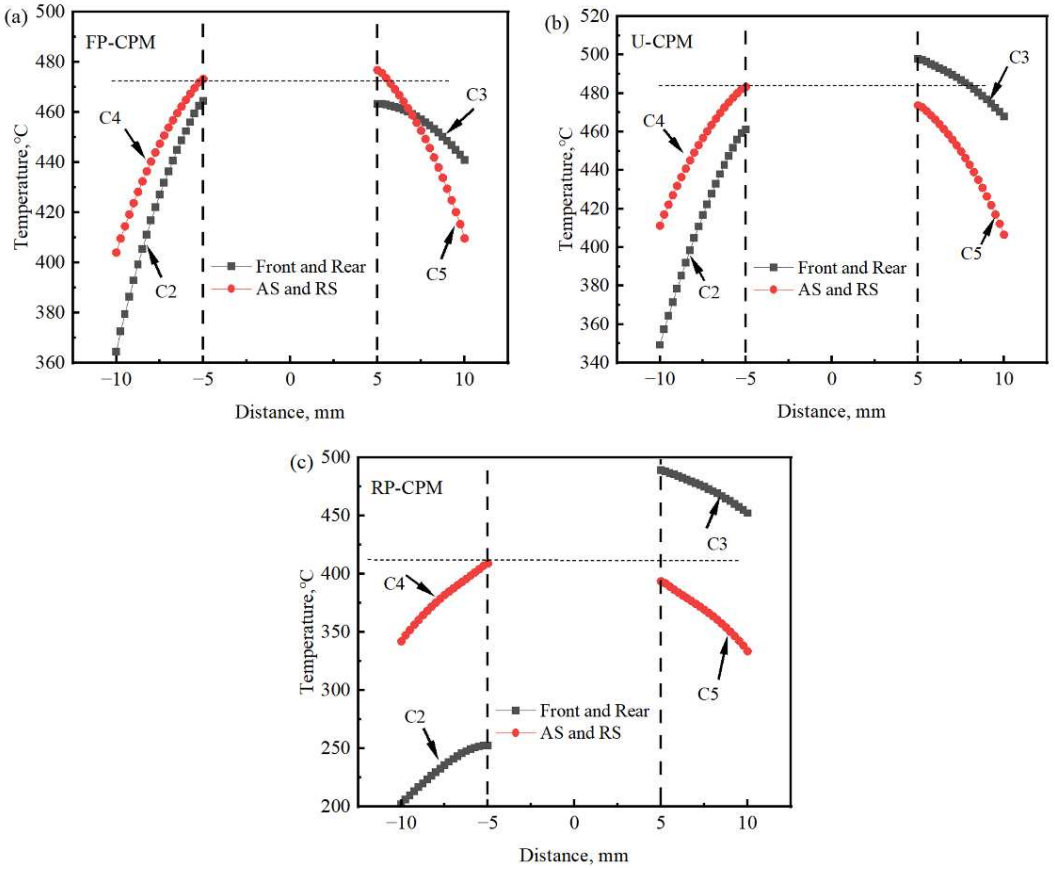


Fig. 12 Temperature comparison of curves C2–C5 under three CPMs

4.2. Heat Generation

To further investigate the origin of the temperature differences among the three models, Figs. 13 and 14 present the heat flux density distributions of frictional heat generation and plastic deformation heat generation, respectively. For the FP-CPM, the heat flux density of frictional heat generation exhibited a non-uniform distribution (Fig. 13a). Higher frictional heat generation occurred ahead of the tool, while lower contact pressure behind the tool resulted in correspondingly reduced frictional heat generation. The heat flux density of frictional heat generation for the U-CPM assumed an annular distribution. At the outer edge of the shoulder, the material flow stress exceeded the frictional shear stress (Fig. 13b), and frictional heat generation dominated. As the radial distance decreased, the material flow stress declined, the frictional shear stress exceeded the material flow stress, frictional heat generation decreased, and material flow commenced. The frictional heat generation for the RP-CPM (Fig. 13c) also exhibited a non-uniform distribution, with higher frictional heat generation behind the tool than ahead of it.

Fig. 14 presents the heat flux density distributions of plastic deformation heat generation on the X = 0 and Y = 0 cross-sections for the three models. In the FP-CPM and U-CPM, the heat flux density of plastic deformation heat generation was primarily distributed around the tool, with distinctly higher values at the upper and lower shoulders than at the pin. Specifically, in the FP-CPM, the lower contact pressure behind the tool resulted in negligible plastic deformation of the material, leading to extremely low plastic heat generation in this region. Simultaneously, the width of plastic deformation on the RS was markedly greater than that on the AS. Using a threshold of 6.0×10^8 W/m³, the widths of the plastic deformation heat generation regions shown in Fig. 14a were 3.51 mm on the RS and 1.25 mm on the AS. In contrast, the plastic heat generation around the tool in the U-CPM was relatively uniform. The widths of the plastic deformation heat generation regions shown in Fig. 14b were 4.05 mm on the RS and 3.49 mm on the AS. The plastic heat generation in the RP-CPM was markedly lower.

In summary, the non-uniform contact pressure exerts a significant influence on frictional heat generation and plastic heat generation. Under the FP-CPM, the higher frictional heat generation ahead of the tool elevates the temperature. Under the rotational action of the tool, the material undergoes further plastic flow toward the RS. This constitutes the primary cause of the higher temperature on the RS than on the AS during the welding process. Fig. 15 presents the statistical results of frictional heat generation, plastic deformation heat generation, and total heat generation for the three models. Owing to the different interfacial contact pressures among the three models, the heat generation mechanisms and total heat generation during the welding process differ. Overall, however, frictional heat generation dominates in all three models. The frictional heat generation of the FP-CPM exceeded that of the U-CPM, whereas the plastic deformation heat generation of the FP-CPM was lower than that of the U-CPM. Both the plastic deformation heat generation and total heat generation of the RP-CPM were the lowest. This explains why the three different contact pressure models produce different effects on the asymmetric distribution of the temperature field. Despite the differences in heat generation mechanisms, the variation in total heat generation was relatively small. The difference in total heat generation between the FP-CPM and U-CPM was within 3.1%, and that between the FP-CPM and RP-CPM was within 13.2%.

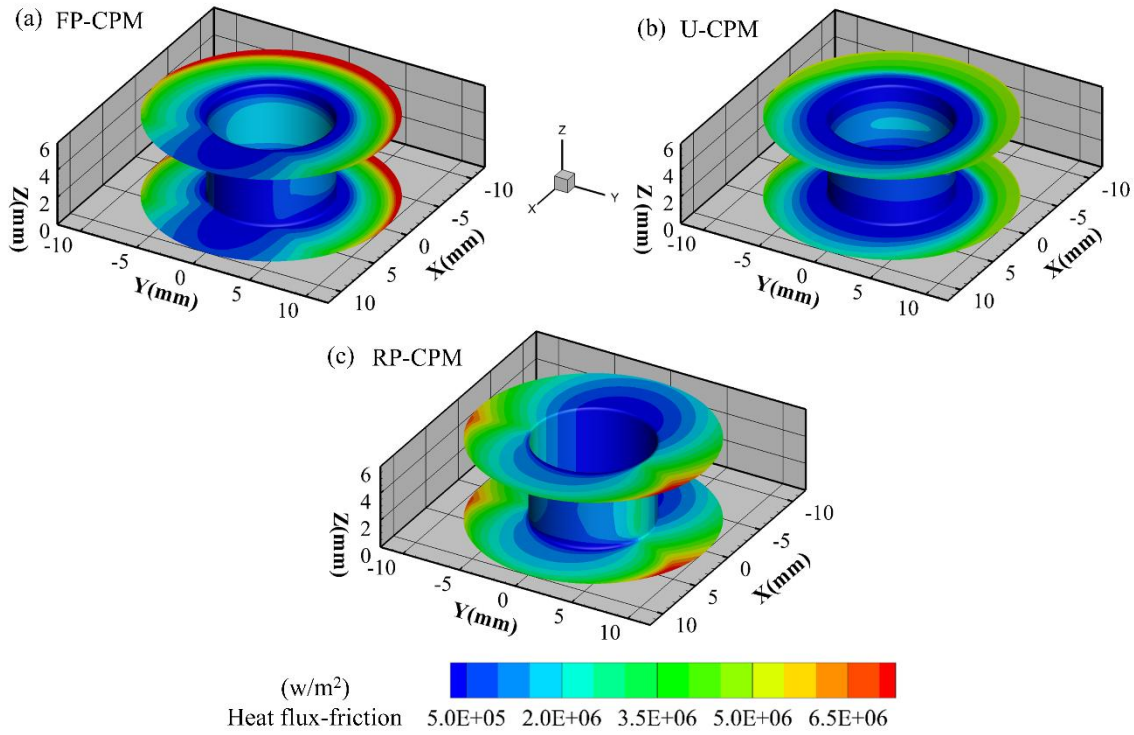


Fig. 13 Heat flux distributions of frictional heat at the T/W interface

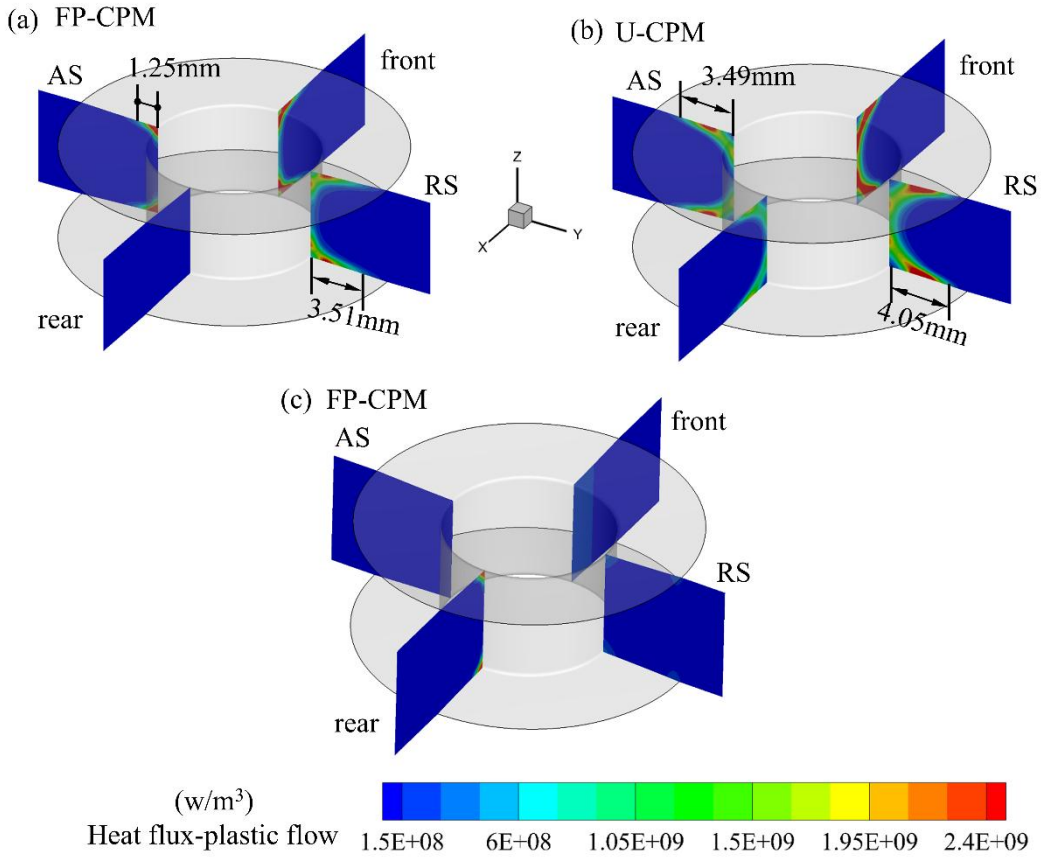


Fig. 14 Heat flux distributions of plastic deformation heat in the vicinity of the T/W interface

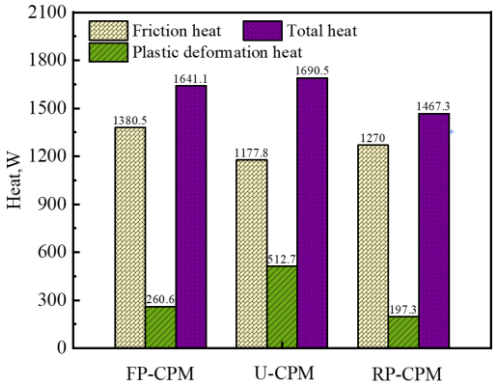


Fig. 15 Heat generation for the different interfacial interaction models

4.3 Material flow behavior

Fig. 16 presents the distribution of material flow velocity at the T/W interface for the three CPMs. In the FP-CPM, the material flow velocity exhibited asymmetry, with higher flow rates on the RS than on the AS. In the U-CPM, the material flow velocity exhibited approximate symmetry, with higher flow rates near the pin region on the shoulder. At the shoulder periphery, the material temperature decreased, and the shear stress was insufficient to overcome the material flow stress. Consequently, the flow velocity was relatively low. In the RP-CPM, the material flow capability was comparatively poor. In the present study, the CFD model was symmetric in configuration, and the material flow at the upper and lower shoulders exhibited symmetry. Therefore, Fig. 17 presents the velocity vector distribution maps on four typical horizontal planes at Z = 5.5 mm, Z = 5 mm, Z = 4 mm, and Z = 3 mm. Near the upper shoulder (Figs. 17a and 17b), the FP-CPM exhibited the most pronounced asymmetric flow characteristics. At the AS and the front region of the shoulder, the coupled action of strong shear from the upper shoulder and tool advancement generated an extremely thin yet high-velocity shear layer. The material flow velocity reached 60 to 100 mm/s. This high-velocity zone adhered closely to the leading edge of the tool and assumed a crescent-shaped distribution. At the RS and the rear region of the shoulder, the contact pressure gradually decreased, the shear stress declined, and the material flow velocity rapidly decreased to 20 to 40 mm/s. Nevertheless, the horizontal flow range of the material was relatively wide, extending toward the rear of the shoulder and depositing. Owing to the reduction in contact pressure and the consequent decrease in shear stress, the material flow gradually weakened. During tool advancement, the material continuously filled the rear region. This phenomenon is consistent with the observation of shear layer flow near the tool reported in Ref.

[54]. As the cross-section moved downward (Figs. 17c and 17d), the material flow velocity decreased closer to the plate mid-thickness plane. The high-velocity shear layer on the AS and at the front gradually thinned, transitioning from a wide crescent-shaped configuration at Z = 5.5 mm to a narrow band at Z = 4 mm. This transition indicates a shift from shoulder-driven to pin-driven flow. The rear region of the tool was dominated by low-velocity zones. Although the material flow width contracted slightly, it maintained a clear trend of extending toward the rear of the tool and depositing.

In contrast, the U-CPM presented approximately concentric annular high-velocity zones centered on the tool at all cross-sections (Figs. 17e through 17h). The flow widths at the rear and on the RS exceeded those of the FP-CPM throughout the entire thickness. This occurs because the uniform contact pressure prevented a significant reduction in shear stress behind the tool, and the material maintained relatively strong circumferential flow characteristics at the rear. The material flow velocity behind the tool in the U-CPM was markedly higher than that in the FP-CPM. The higher temperature at point C3 in the U-CPM than in the FP-CPM shown in Fig. 12 corroborates this phenomenon, indicating that the non-uniform temperature distribution exerts a significant influence on material flow. In the thickness direction, the U-CPM exhibited overall contraction of the annular zone as the cross-section approached the tool center plane, which differs markedly from the asymmetric decay observed in the FP-CPM. In the RP-CPM (Figs. 17i through 17l), the absence of a high-velocity shear layer on the AS and at the front suppressed material flow. This implies that the material ahead of the tool was not effectively entrained and deposited behind the tool during advancement, resulting in a reduced material flow width behind the tool. Consequently, the FP-CPM exhibited an asymmetric characteristic featuring a thin high-velocity flow layer ahead of the tool and a broader low-velocity flow region behind it. This characteristic produced a rear material flow width that fell between that of the U-CPM (excessively wide) and that of the RP-CPM (excessively narrow).

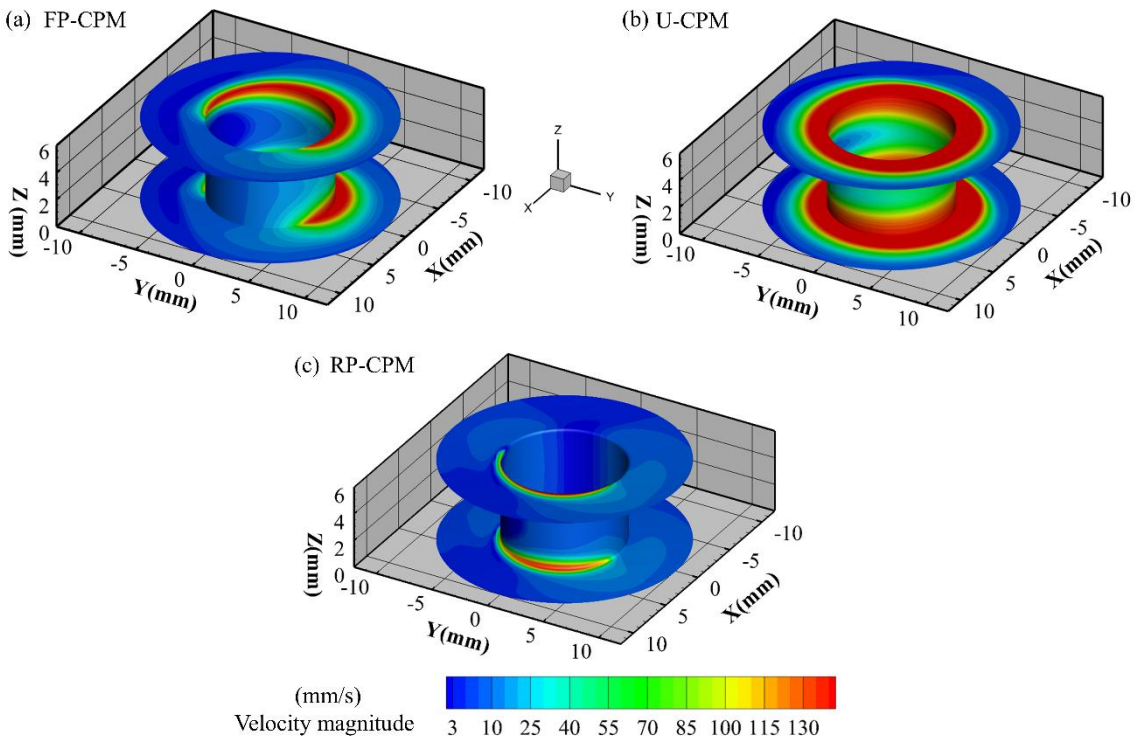


Fig. 16 Material flow velocity distribution around the tool

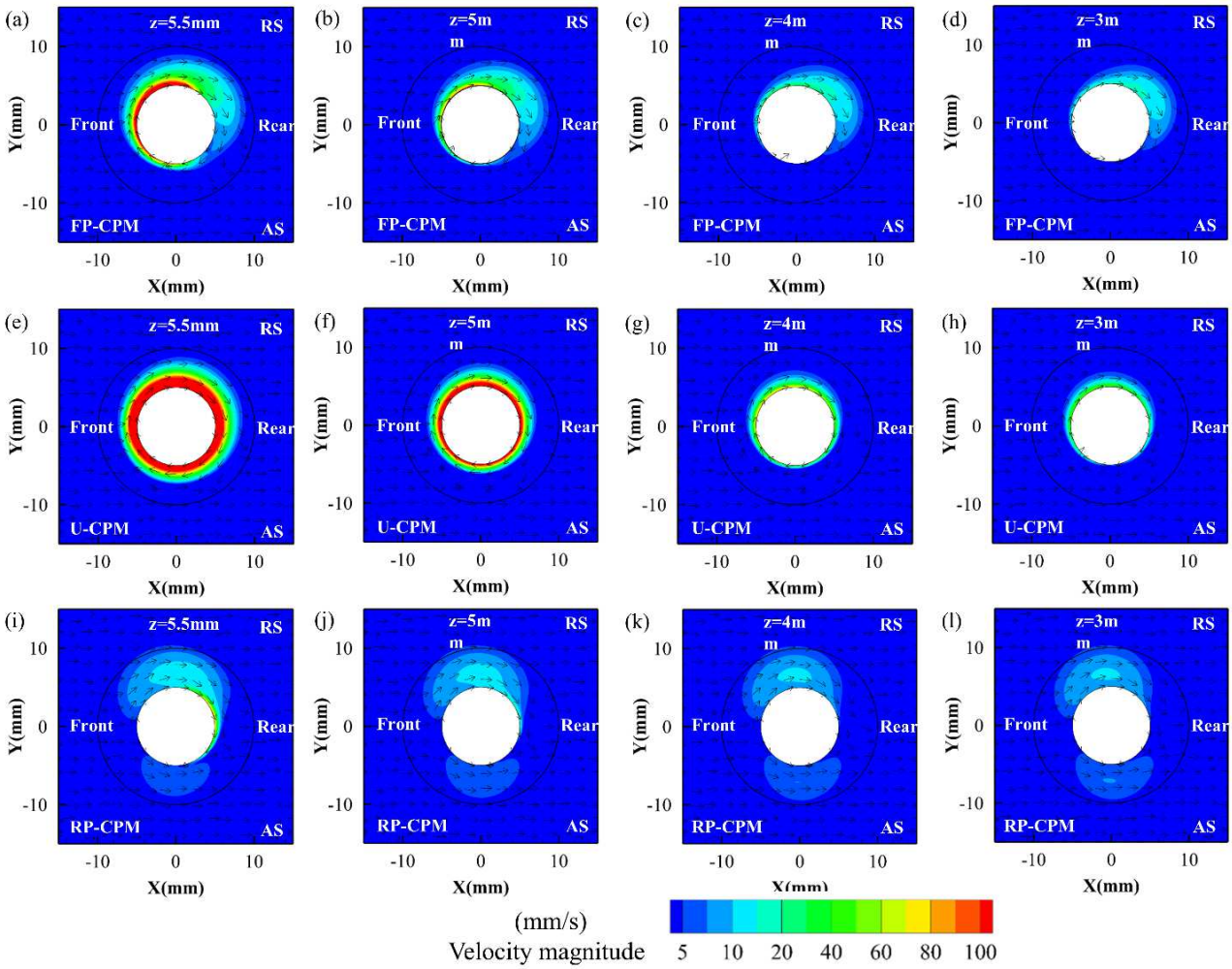


Fig. 17 Velocity distributions on horizontal planes

Fig. 18 presents the material flow velocities extracted along four curves on the shoulder surface, indicated by blue dashed lines in the figure. In the rear region of the tool under the FP-CPM, the material flow velocity was relatively low, with a maximum value of 10.3 mm/s. Outside this rear region, as the material approached the tool root from the shoulder periphery under the FP-CPM, the flow velocity increased rapidly. In the region enclosed by the black dashed box in the figure, the material clearly exhibited the sticking state. Figs. 19 and 20 present the slip rates extracted on the shoulder and the pin, respectively. The blue dashed lines in the figures indicate the data extraction positions on the tool. Fig. 19 reveals that the material at the shoulder periphery remained in the sliding state for all three CPMs. As the material moved from the shoulder periphery toward the tool root, it gradually transitioned into the sliding-sticking state and approached the fully sticking state near the tool root. In contrast, the material in the U-CPM transitioned from the sliding state to the sliding-sticking state more

rapidly. This more satisfactorily explains the phenomenon that the frictional heat generation of the FP-CPM exceeded that of the U-CPM, whereas the plastic deformation heat generation of the U-CPM exceeded that of the FP-CPM. In the rear region of the FP-CPM, the slip rate remained between 0.9 and 1.0, indicating that the material in this region remained in the sliding state throughout. In the RP-CPM, a small amount of sliding-sticking state existed at the rear of the shoulder, while other regions remained basically in the sliding state due to the low material flow velocity. Fig. 20 reveals that the closer the material on the pin approached the pin midsection, the more pronounced the sliding state became. For both the FP-CPM and the U-CPM, the sliding state at the rear was more pronounced than that at the front, and the sliding state on the RS was also more pronounced than that on the AS.

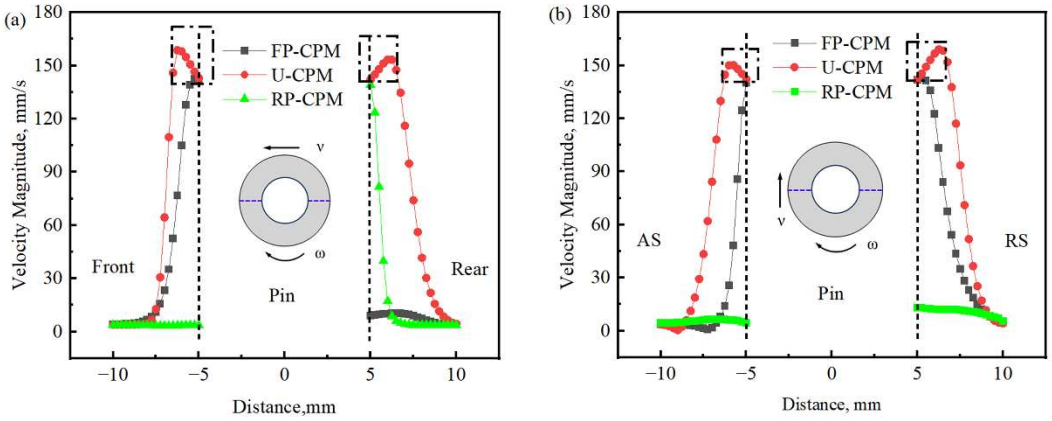


Fig. 18 Velocity distribution of material next to the shoulder

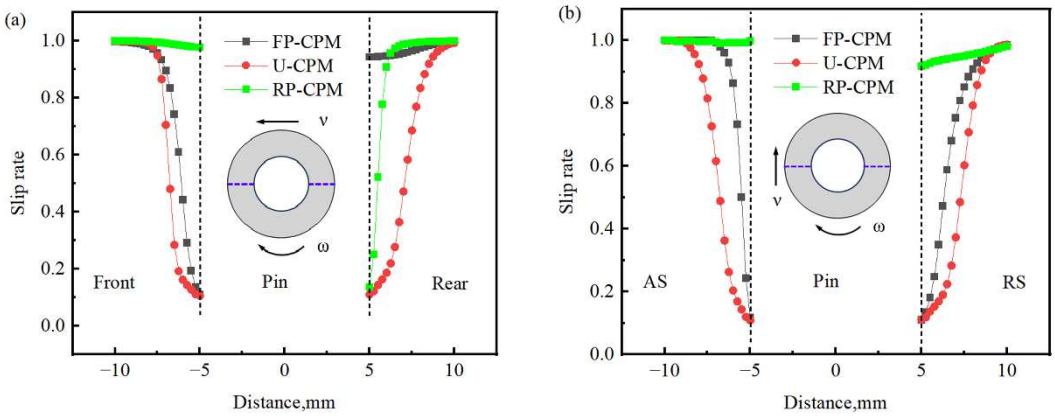


Fig. 19 Slip rate distribution on the shoulder

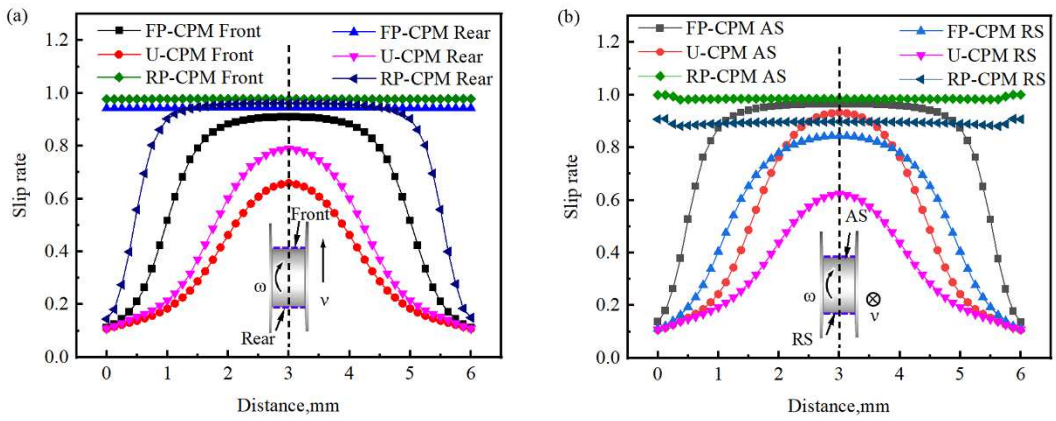


Fig. 20 Slip rate distribution at the pin

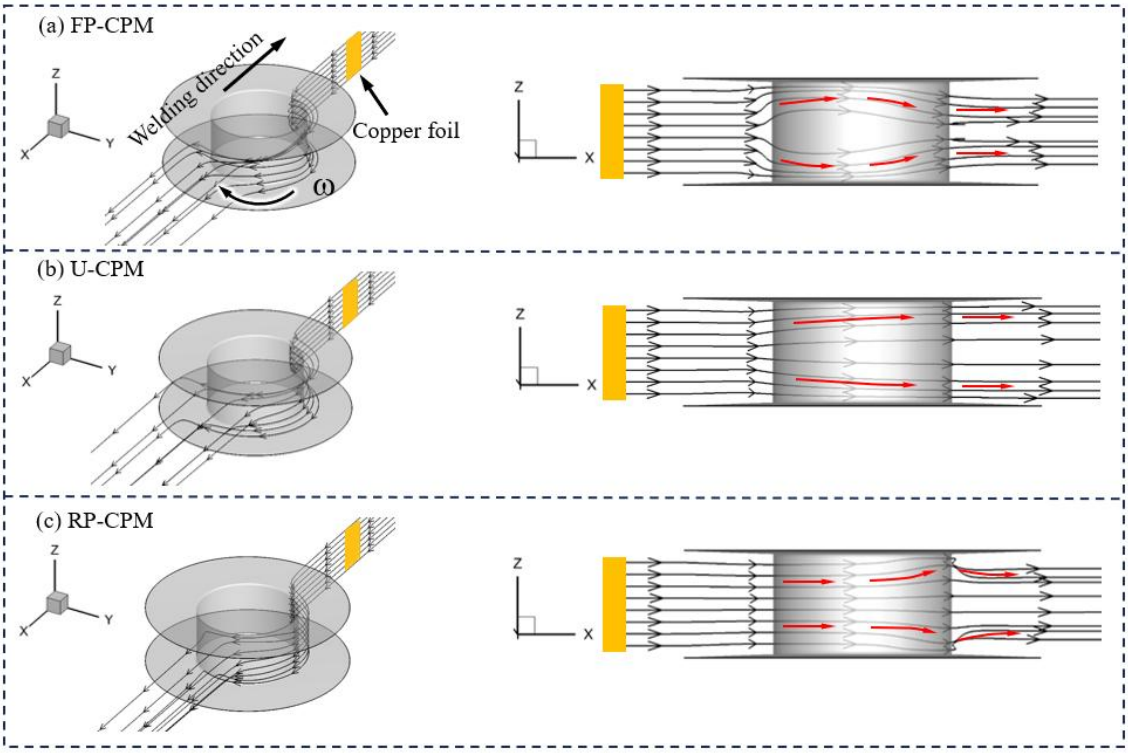


Fig. 21 Flow trajectories of copper particles

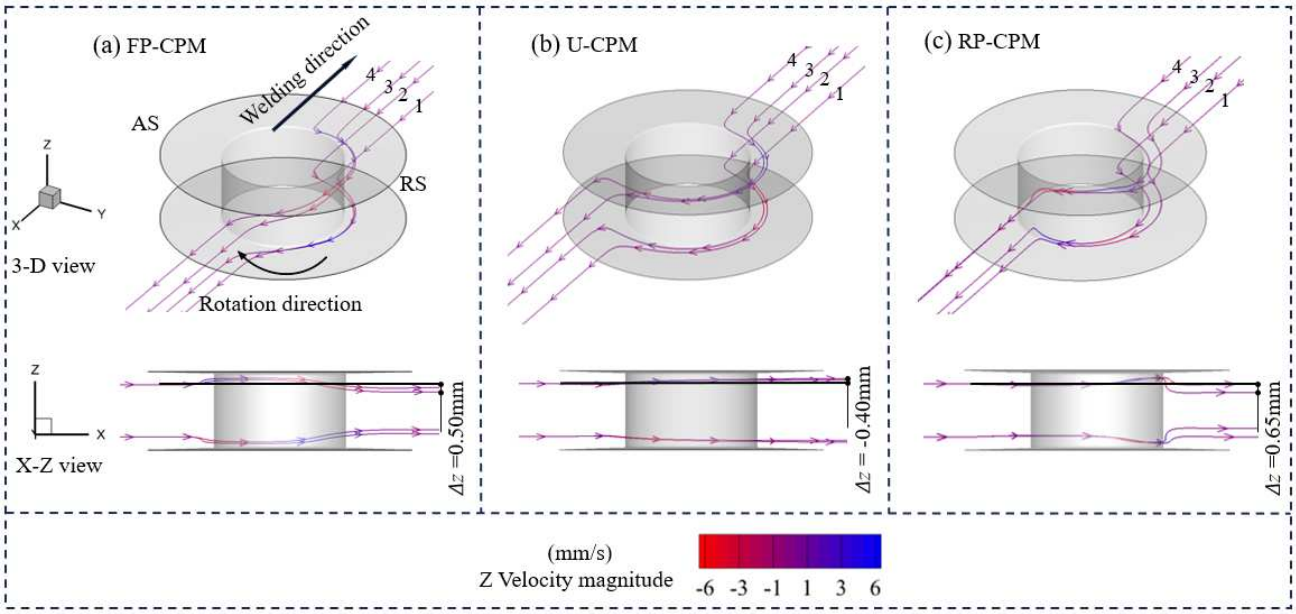


Fig. 22 Flow paths of representative streamlines and their Z-direction velocity

Fig. 21 presents the predicted flow trajectories of the copper tracer. The copper tracer was placed on the butt interface ahead of the tool, consistent with the experimental configuration. Fig. 21 reveals that in all three CPMs, the copper tracer particles rotated around the tool and ultimately deposited behind the tool. All cases exhibited pronounced vertical flow. In the FP-CPM (Fig. 21a), after flowing past the tool, the material first flowed upward near the upper shoulder and downward near the lower shoulder, and subsequently reversed direction to flow downward near the upper shoulder and upward near the lower shoulder under the combined action of the upper and lower shoulders and the pin. Overall, the material exhibited a characteristic circumferential flow around the tool with convergence toward the plate mid-thickness. This phenomenon was also observed in experiments [36,63]. In contrast, in the U-CPM (Fig. 21b), the copper tracer particles flowed slightly upward after passing the tool and subsequently deposited behind the tool. The vertical flow in the U-CPM was weaker than that in the FP-CPM. In the RP-CPM (Fig. 21c), the flow trajectories of the copper tracer material under the tool action were similar to those in the FP-CPM. Fig. 22 presents the flow trajectories of four typical streamlines at Y = ±1 mm and Z = 1 mm, and Y = ±1 mm and Z = 5 mm. In the FP-CPM (Fig. 22a) and the RP-CPM (Fig. 22c), the streamlines converged toward the plate mid-thickness, with maximum Z-direction displacements of 0.50 mm and 0.65 mm, respectively. In the U-CPM (Fig. 22b), although the streamlines also exhibited a tendency for vertical flow, the direction was toward the top or bottom

surface of the plate, with a displacement of 0.40 mm (the negative sign in the figure indicates the opposite flow direction). The predicted material flow trajectories indicate that the non-uniform contact pressure exerts a significant influence on material flow. To further validate the accuracy of the predicted material flow trajectories, Fig. 23 presents the distribution of the copper tracer on the butt interface of the two plates after stirring, and this distribution is compared with the experimentally observed copper tracer distribution. Fig. 23d presents the copper tracer distribution obtained through the X-ray digital imaging system. The particles were primarily distributed within the 13.2 mm interval indicated by the red solid line on the center plane of the butt interface behind the tool. The spatial extent of the copper tracer distribution on the AS (8.5 mm) exceeded that on the RS (4.7 mm). Figs. 23a through 23c present the predicted particle distributions on the butt interface for the three CPMs. The post-weld particle distribution predicted by the FP-CPM exhibited superior agreement with the experimental results. In the U-CPM, some copper tracer particles extended beyond the experimentally observed distribution range. The RP-CPM exhibited substantial deviation from the experimental results. This indicates that the FP-CPM more accurately predicts the material flow behavior.

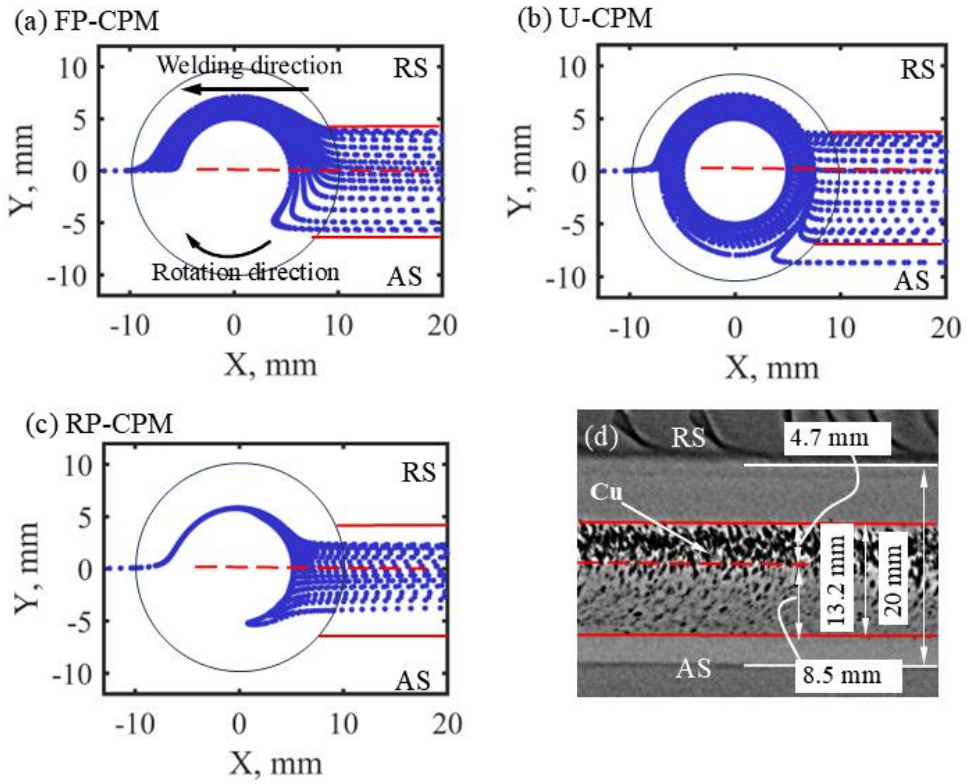


Fig. 23 Comparison of experimental and predicted copper particle distributions after welding

4.4. Plastic Deformation Zone

Macroscopic examination of BT-FSW joints typically reveals the boundaries of the Thermo-Mechanically Affected Zone (TMAZ) on both sides of the weld, with the TMAZ boundary on the AS appearing more distinct than that on the RS [1,64]. To accurately characterize the predicted morphology of the joint TMAZ, the present study employed the particle tracking method. As shown in Fig. 24, 4650 tracer particles were uniformly distributed on the YZ cross-section (30 mm × 6 mm) at the inflow boundary. These particles flowed in the positive X-direction past the tool, and an observation plane was established behind the tool where the particles were ultimately deposited.

Fig. 25a presents the experimental macroscopic morphology of the joint; the black dashed line indicates the TMAZ boundary. Figs. 25b through 25d present the deposited morphologies of the deflected tracer particles on the observation plane. The equivalent strain rate of the material flow was calculated using Equations (17) through (18), and the deposited particle flow paths were determined using a threshold of 1 s^{-1}.

The results reveal that the material exhibited a symmetric distribution about the plate mid-thickness plane under the action of the upper and lower shoulders. The deposited morphology of the tracer particles assumed a dumbbell-shaped configuration. The predicted deposition positions of the tracer particles in the FP-CPM exhibited superior agreement with the experimental results compared with those in the U-CPM and the RP-CPM. The U-CPM exhibited a wider plastic deformation zone in the shoulder region. This further demonstrates that the contact pressure distribution exerts a significant regulatory effect on plastic deformation localization. The FP-CPM more accurately captures the characteristics of the plastic deformation zone during the BT-FSW process.

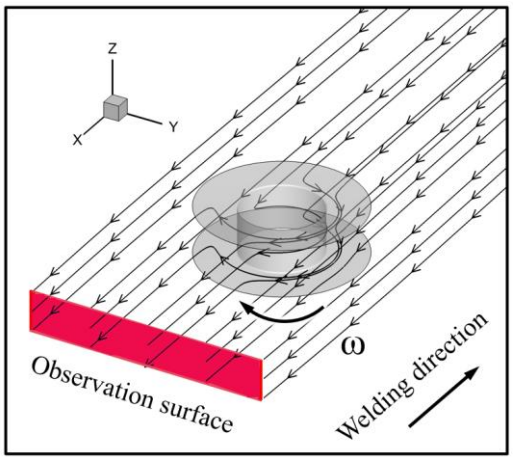


Fig. 24 Particle tracking method

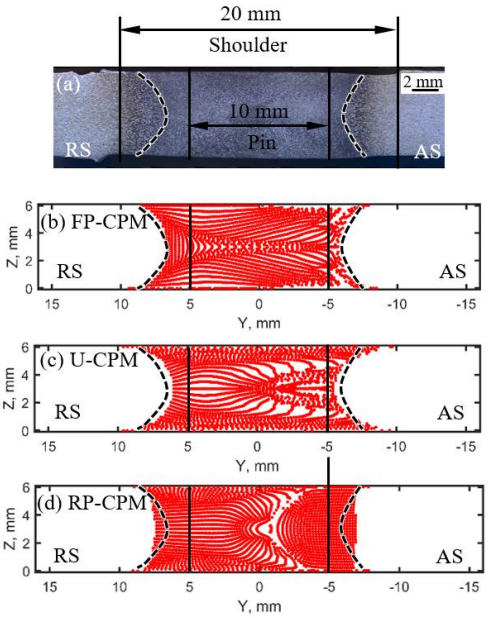


Fig. 25 Comparison of macroscopic TMAZ morphologies of the joint

Conclusions

The present study proposes a non-uniform contact pressure model incorporating T/W interfacial interaction for the BT-FSW process, and establishes a fully coupled thermo-mechanical-fluid numerical simulation method based on CFD. The method is employed to predict the distributions of the temperature field, flow trajectories, and plastic deformation zones. The main conclusions are drawn as follows:

(1) The contact pressure distribution at the T/W interface constitutes a critical factor governing the spatial characteristics of the temperature field and material flow behavior during the BT-FSW process. The FP-CPM accurately predicts the temperature field distribution, flow trajectories, and geometric characteristics of plastic deformation zones during the welding process.

(2) The temperature evolution during the welding process and elucidates that the elevated temperature on the RS in BT-FSW arises from the migration of high-temperature material toward the RS driven by the high-pressure zone ahead of the tool, thereby inducing RS temperature rise.

(3) The FP-CPM reveals the asymmetric flow characteristic near the T/W interface, manifested as a thin high-velocity layer ahead of the tool and a broader low-velocity region behind it in the horizontal direction, as well as the vertical migration pattern in which material flows circumferentially

around the tool and converges toward the plate mid-thickness.

Acknowledgement

The research was financially supported by the National Natural Science Foundation of China (No. 52175334).

References

1. Rezende GN, Bernardi M, Hoffmann M, Bergmann L, Zepon G, Klusemann B (2025) Enhancement of the mechanical properties of semi-stationary bobbin tool friction stir welded joints in AA2219 through post-weld heat treatment. Mater Sci Eng A 920:147498. https://doi.org/10.1016/j.msea.2024.147498
2. Feng J, Liu W, Li Y, Gong W, Zhu R, Liu J (2024) Effect of heat input on the temperature and microstructures of bobbin-tool-friction-stir-welded 6061-T6 aluminum alloy thick plate. Int J Adv Manuf Technol 135:2131-2144. https://doi.org/10.1007/s00170-024-14519-2
3. Balos S, Labus Zlatanovic D, Kulundzic N, Janjatovic P, Dramicanin M, Lanc Z, Hadzistevic M, Radisic S, Rajnovic D, Pecanac M (2023) Influence of Tool–Base Metal Interference on the Performance of an Aluminium–Magnesium Alloy Joined via Bobbin Tool Friction Stir Welding. Metals 13:1215-1231. https://doi.org/https://doi.org/10.3390/met13071215
4. Kumar S, Maurya M, Bansal S, Aniruddha (2024) Influence of Bobbin Tool on Microstructure, Residual Stress, Tool and Corrosion Analysis of Al 6063 Alloy Friction Stir Welded Joint. J Mater Eng Perform 14:14199-14211. https://doi.org/10.1007/s11665-024-10244-9
5. Feng J, Gong W, Li Y, Liu W, Liu J, Su X, Zhang J, Liu W (2025) Microstructure and texture evolution in bobbin tool friction stir welded 16mm-thick 6061-T4 aluminum alloy: Investigation into the correlation with mechanical behavior. Mater Today Commun 46:112544. https://doi.org/10.1016/j.mtcomm.2025.112544
6. Wen Q, Li W, Patel V, Gao Y, Vairis A (2019) Investigation on the Effects of Welding Speed on Bobbin Tool Friction Stir Welding of 2219 Aluminum Alloy. Met Mater Int 26:1830-1840. https://doi.org/10.1007/s12540-019-00450-9
7. Mirabzadeh R, Parvaneh V, Ehsani A (2021) Experimental and numerical investigation of the generated heat in polypropylene sheet joints using friction stir welding (FSW). Int J Mater Form 14:1067-1083. https://doi.org/10.1007/s12289-021-01622-y
8. Zhao P, Gao J, Yuan T, Shan H, Wang S, Chen S (2025) Experimental and numerical investigation on mesoscopic damage evolution behavior of dissimilar friction stir welded AA2024/7075 joints. Int J Mater Form 18:99. https://doi.org/10.1007/s12289-025-01961-0
9. Wang G-Q, Zhao Y-H, Tang Y-Y (2019) Research Progress of Bobbin Tool Friction Stir Welding of Aluminum Alloys: A Review. Acta Metall Sin-engl 33:13-29. https://doi.org/10.1007/s40195-019-00946-8
10. Chen G, Zhang S, Zhu Y, Yang C, Shi Q (2019) Thermo-mechanical Analysis of Friction Stir Welding: A Review on Recent Advances. Acta Metall Sin-engl 33:3-12.

https://doi.org/10.1007/s40195-019-00942-y
11. Liu FC, Hovanski Y, Miles MP, Sorensen CD, Nelson TW (2018) A review of friction stir welding of steels: Tool, material flow, microstructure, and properties. J Mater Sci Technol 34:39-57. https://doi.org/10.1016/j.jmst.2017.10.024
12. Schmidt H, Hattel J, Wert J (2004) An analytical model for the heat generation in friction stir welding. Model Simul Mater Sc 12:143-157. https://doi.org/10.1088/0965-0393/12/1/013
13. Zhang HJ, Liu HJ, Yu L (2013) Thermal modeling of underwater friction stir welding of high strength aluminum alloy. T Nonferr Metal Soc 23:1114-1122. https://doi.org/10.1016/S1003-6326(13)62573-X
14. Kumar R, Pancholi V (2021) Three-dimensional material flow during friction stir welding of AA5083. J Manuf Process 68:1214-1223. https://doi.org/10.1016/j.jmapro.2021.06.051
15. Morisada Y, Imaizumi T, Fujii H, Matsushita M, Ikeda R (2014) Three-Dimensional Visualization of Material Flow During Friction Stir Welding of Steel and Aluminum. J Mater Eng Perform 23:4143-4147. https://doi.org/10.1007/s11665-014-1202-6
16. Aziz SB, Dewan MW, Huggett DJ, Wahab MA, Okeil AM, Liao TW (2017) A Fully Coupled Thermomechanical Model of Friction Stir Welding (FSW) and Numerical Studies on Process Parameters of Lightweight Aluminum Alloy Joints. Acta Metall Sin-engl 31:1-18. https://doi.org/10.1007/s40195-017-0658-4
17. Salloomi KN (2019) Fully coupled thermomechanical simulation of friction stir welding of aluminum 6061-T6 alloy T-joint. J Manuf Process 45:746-754. https://doi.org/10.1016/j.jmapro.2019.06.030
18. Zhou Y, Wang J, Zhao Y, Cheng L, Zhan X (2023) Numerical analysis of coupling dynamics of keyhole and molten pool in vertical-up laser mirror welding of 2219 aluminum alloy. Int J Therm Sci 192:108390. https://doi.org/10.1016/j.ijthermalsci.2023.108390
19. Shi L, Chen J, Yang C, Chen G, Wu C (2023) Thermal-fluid-structure coupling analysis of void defect in friction stir welding. Int J Mech Sci 241:107969. https://doi.org/10.1016/j.ijmecsci.2022.107969
20. Yang C, Dai Q, Shi Q, Wu C, Zhang H, Chen G (2022) Flow-coupled thermo-mechanical analysis of frictional behaviors at the tool-workpiece interface during friction stir welding. J Manuf Process 79:394-404. https://doi.org/10.1016/j.jmapro.2022.05.003
21. Qiao J, Shi Q, Wu C, Chen S, Han Y, Yang C, Chen G (2023) Elucidation of solid-state metal flow behaviors during friction stir welding: Numerical and experimental investigation. Phys Fluids 35:123105. https://doi.org/10.1063/5.0175343
22. Li Y, Yu M, Gao S, Sun G, An H, Zhou L (2025) Quasi-in-situ reconstruction and regulating mechanism of plastic flow in steel friction stir welding. Int J Mach Tool Manu 213:104341. https://doi.org/10.1016/j.ijmachtools.2025.104341
23. Yang C, Chen G, Qiao J, Wu C, Zhou M, Zhang G, Shi Q (2024) Material flow during dissimilar friction stir welding of Al/Mg alloys. Int J Mech Sci 272:109173. https://doi.org/10.1016/j.ijmecsci.2024.109173
24. Zhang S, Shi Q, Liu Q, Xie R, Zhang G, Chen G (2018) Effects of tool tilt angle on the in-process heat transfer and mass transfer during friction stir welding. Int J Heat Mass Tran 125:32-42. https://doi.org/10.1016/j.ijheatmasstransfer.2018.04.067

25. Zhao P-c, Shen Y-f, Huang G-q, Zheng Q-x (2018) Numerical simulation of friction stir butt-welding of 6061 aluminum alloy. T Nonferr Metal Soc 28:1216-1225. https://doi.org/10.1016/s1003-6326(18)64759-4
26. Cho H-H, Hong S-T, Roh J-H, Choi H-S, Kang SH, Steel RJ, Han HN (2013) Three-dimensional numerical and experimental investigation on friction stir welding processes of ferritic stainless steel. Acta Mater 61:2649-2661. https://doi.org/10.1016/j.actamat.2013.01.045
27. Su H, Wu CS, Pittner A, Rethmeier M (2014) Thermal energy generation and distribution in friction stir welding of aluminum alloys. Energy 77:720-731. https://doi.org/10.1016/j.energy.2014.09.045
28. Chen G, Ma Q, Zhang S, Wu J, Zhang G, Shi Q (2018) Computational fluid dynamics simulation of friction stir welding: A comparative study on different frictional boundary conditions. J Mater Sci Technol 34:128-134. https://doi.org/10.1016/j.jmst.2017.10.015
29. Yadav A, Jain A, Verma R (2023) Effect of tilt angle for conical pin tool with a conical shoulder on heat transfer and material flow using numerical simulation in friction stir welding. Mater Phys Mech 51:126-145. https://doi.org/10.18149/MPM.5132023_14
30. Yin P, Zhang R, Xiong J, Li J (2013) Numerical simulation of coupled thermo-mechanical process of friction stir welding in quasi-steady-state. Acta Phys Sin-CH 62:480-487. https://doi.org/10.7498/aps.62.018102
31. Wu CS, Su H, Shi L (2018) Numerical Simulation of Heat Generation, Heat Transfer and Material Flow in Friction Stir Welding. Acta Metall Sin 54:265-277. https://doi.org/10.11900/0412.1961.2017.00294
32. Singh P, Biswas P, Kore SD (2016) A three-dimensional fully coupled thermo-mechanical model for Self-reacting Friction Stir Welding of Aluminium AA6061 sheets. J Phys Conf Ser 759:012047. https://doi.org/10.1088/1742-6596/759/1/012047
33. Li Y, Sun D, Gong W (2019) Temperature fields in bobbin-tool friction stir welding for 6082-T6 aluminum alloy sheet. J Jilin Univ Eng Technol Ed 49:836-841. https://doi.org/10.13229/j.cnki.jdxbgxb20180202
34. Sun Y, Liu W, Li Y, Sun S, Gong W (2023) Study on temperature field, microstructure, and properties of T2 pure copper by bobbin tool friction stir welding. Int J Adv Manuf Technol 127:1341-1353. https://doi.org/10.1007/s00170-023-11650-4
35. Li G, Gao S, Luo S, Zhou L, Zhang X, Cui F, Zhao H, Feng X (2024) Tailoring macrostructure and texture in bobbin-tool friction stir weld via manipulation of deformation behaviour of plasticised metal during welding enabled by modifying tool profile. Int J Mach Tool Manu 201:104198. https://doi.org/10.1016/j.ijmachtools.2024.104198
36. Feng J, Gong W, Liu W, Li Y, Zhu R (2024) The evolution of thermal cycle, microstructures and mechanical properties of 6061 – T6 aluminum alloy thick plate Bobbin tool friction stir welded. Int J Mater Form 17:61. https://doi.org/10.1007/s12289-024-01863-7
37. Zhao C, Liu X (2021) An alternative pressure-dependent velocity boundary condition for modeling self-reacting friction stir welding. Int J Adv Manuf Technol 117:1601-1613. https://doi.org/10.1007/s00170-021-07589-z
38. Hasan AF, Bennett CJ, Shipway PH, Cater S, Martin J (2017) A numerical methodology for predicting tool wear in Friction Stir Welding. J Mater Process Tech 241:129-140.

https://doi.org/10.1016/j.jmatprotec.2016.11.009
39. Chen G, Feng Z, Zhu Y, Shi Q (2016) An Alternative Frictional Boundary Condition for Computational Fluid Dynamics Simulation of Friction Stir Welding. J Mater Eng Perform 25:4016-4023. https://doi.org/10.1007/s11665-016-2219-9
40. Zhang Z, Zhang HW (2007) Numerical studies on effect of axial pressure in friction stir welding. Sci Technol Weld Joi 12:226-248. https://doi.org/10.1179/174329307x177919
41. Zhang Z, Wu Q (2015) Analytical and numerical studies of fatigue stresses in friction stir welding. Int J Adv Manuf Technol 78:1371-1380. https://doi.org/10.1007/s00170-014-6749-8
42. Zhang Z, Wu Q, Zhang HW (2016) Prediction of fatigue life of welding tool in friction stir welding of AA6061-T6. Int J Adv Manuf Technol 86:3407-3415. https://doi.org/10.1007/s00170-016-8475-x
43. Dialami N, Chiumenti M, Cervera M, Segatori A, Osikowicz W (2017) Enhanced friction model for Friction Stir Welding (FSW) analysis: Simulation and experimental validation. Int J Mech Sci 133:555-567. https://doi.org/10.1016/j.ijmecsci.2017.09.022
44. Long L, Chen G, Zhang S, Liu T, Shi Q (2017) Finite-element analysis of the tool tilt angle effect on the formation of friction stir welds. J Manuf Process 30:562-569. https://doi.org/10.1016/j.jmapro.2017.10.023
45. Pei X, Dong P (2017) An improved friction stir shear localization model and applications in understanding weld formation process in alloy Ti-6-4. Int J Adv Manuf Technol 95:3549-3562. https://doi.org/10.1007/s00170-017-1467-7
46. Zhai M, Wu C, Su H (2020) Influence of tool tilt angle on heat transfer and material flow in friction stir welding. J Manuf Process 59:98-112. https://doi.org/10.1016/j.jmapro.2020.09.038
47. Meyghani B, Awang M (2022) The Influence of the Tool Tilt Angle on the Heat Generation and the Material Behavior in Friction Stir Welding (FSW). Metals 12:1837. https://doi.org/10.3390/met12111837
48. Fan G, Tomków J, Abdullah ME, Derazkola HA (2023) Investigation on polypropylene friction stir joint: effects of tool tilt angle on heat flux, material flow and defect formation. J Mater Res Technol 23:715-729. https://doi.org/10.1016/j.jmrt.2023.01.028
49. Ke L, Pan J, Xing l, Wang S (2009) Sucking-extruding Theory for the Material Flow in Friction Stir Welds. J Mech Eng 45:89-94. https://doi.org/CNKI:SUN:JXXB.0.2009-04-017
50. He C, Qie M, Zhang Z, Zhao x (2021) Effect of Axial Ultrasonic Vibration on Metal Flow Behavior During Friction Stir Welding. Acta Metall Sin 57:1614-1626. https://doi.org/10.11900/0412.1961.2021.00288
51. Han HH, Shi QY, Yang CL, Kong DS, Chen GQ (2026) Coupled Thermal-Mechanical-Fluid Simulation and Material Migration Trajectory Analysis for Friction Stir Welding of Aluminum Alloy. Acta Metall Sin 62:148-158. https://doi.org/10.11900/0412.1961.2025.00240
52. Chen G, Wang G, Shi Q, Zhao Y, Hao Y, Zhang S (2019) Three-dimensional thermal-mechanical analysis of retractable pin tool friction stir welding process. J Manuf Process 41:1-9. https://doi.org/10.1016/j.jmapro.2019.03.022
53. Chen J, Wang X, Shi L, Wu C, Liu H, Chen G (2023) Numerical simulation of weld formation in friction stir welding based on non-uniform tool-workpiece interaction: An effect of tool pin size. J Manuf Process 86:85-97. https://doi.org/https://doi.org/10.1016/j.jmapro.2022.12.052
54. Chen ZW, Pasang T, Qi Y (2008) Shear flow and formation of Nugget zone during friction stir

welding of aluminium alloy 5083-O. Mater Sci Eng A 474:312-316. https://doi.org/10.1016/j.msea.2007.05.074
55. Chen G, Shi Q, Li Y, Sun Y, Dai Q, Jia J, Zhu Y, Wu J (2013) Computational fluid dynamics studies on heat generation during friction stir welding of aluminum alloy. Comp Mater Sci 79:540-546. https://doi.org/10.1016/j.commatsci.2013.07.004
56. Bastier A, Maitournam MH, Dang Van K, Roger F (2006) Steady state thermomechanical modelling of friction stir welding. Sci Technol Weld Joi 11:278-288. https://doi.org/10.1179/174329306x102093
57. Su H, Wu CS, Bachmann M, Rethmeier M (2015) Numerical modeling for the effect of pin profiles on thermal and material flow characteristics in friction stir welding. Mater Design 77:114-125. https://doi.org/10.1016/j.matdes.2015.04.012
58. Wang X, Gao Y, Liu X, McDonnell M, Feng Z (2021) Tool-workpiece stick-slip conditions and their effects on torque and heat generation rate in the friction stir welding. Acta Mater 213:116969. https://doi.org/10.1016/j.actamat.2021.116969
59. Atharifar H, Lin D, Kovacevic R (2009) Numerical and Experimental Investigations on the Loads Carried by the Tool During Friction Stir Welding. J Mater Eng Perform 18:339-350. https://doi.org/10.1007/s11665-008-9298-1
60. Wan SQ, Wu YX, Gong H, Nie L (2019) Thermal Mechanical Coupling Simulation of Temperature and Residual Stress in Friction Stir Welding of 2219 Aluminum Alloy. Hot Work Technol 48:159-163. https://doi.org/10.14158/j.cnki.1001-3814.2019.13.042
61. Wang K, Wu YX, Gong H, Liu L (2019) Strain-compensated Constitutive Model for High Temperature Plastic Deformation of 2219 Aluminum Alloy. Hot Work Technol 48:120-124. https://doi.org/10.14158/j.cnki.1001-3814.2019.09.032
62. Jain R, Pal SK, Singh SB (2016) A study on the variation of forces and temperature in a friction stir welding process: A finite element approach. J Manuf Process 23:278-286. https://doi.org/10.1016/j.jmapro.2016.04.008
63. Yu Z, Zhang W, Choo H, Feng Z (2011) Transient Heat and Material Flow Modeling of Friction Stir Processing of Magnesium Alloy using Threaded Tool. Metall Mater Trans A 43:724-737. https://doi.org/10.1007/s11661-011-0862-1
64. Kopyściański M, Dymek S, Hamilton C, Węglowska A, Kalemba-Rec I (2024) Microstructural Characterization of Friction Stir Welds of Aluminum 6082 Produced with Bobbin Tool. Materials 17:4738. https://doi.org/10.3390/ma17194738